AN ABSTRACT OF THE THESIS OF

Anthony L. Alberti for the degree of Master of Science in Nuclear Engineering presented on October 2, 2015.

Title:

Steady State Modeling of the Minimum Critical Core of the Transient Reactor Test Facility

Abstract approved:

Dr. Todd S. Palmer

With the advent of next generation reactor systems and new fuel designs, the U.S. Department of Energy (DOE) has identified the need for the resumption of transient testing of nuclear fuels [30]. The DOE has decided that the Transient Reactor Test Facility (TREAT) at Idaho National Laboratory (INL) is best suited for future testing. TREAT is a thermal neutron spectrum, air-cooled, nuclear test facility that is designed to test nuclear fuels in transient scenarios. These specific scenarios range from simple temperature transients to full fuel melt accidents [9].

DOE desires a simulation capability that will accurately model the experiments before they are irradiated at the facility. It is the aim for this capability to have an emphasis on effective and safe operation while minimizing experimental time and cost. The multiphysics platform MOOSE has been selected as the framework for this project.

The goals of this thesis are to investigate the fundamental neutronics properties of TREAT and to develop an accurate steady state model for future multiphysics transient simulations. To minimize computational cost, the effects of spatial and angular homogenization approaches were investigated. A high degree of anisotropy is present in TREAT assemblies and to capture this effect, explicit modeling of cooling channels and interassembly gaps is necessary. Single assembly calculations at 293K gave power distributions 0.076% different than that of reference Monte Carlo (SERPENT) calculations. The minimum critical core configuration with identical gap and channel treatment at 293K resulted in a root mean square, axially integrated radial power distribution difference of 0.22% compared to reference SERPENT solutions.

Steady State Modeling of the Minimum Critical Core of the Transient Reactor Test Facility

by

Anthony L. Alberti

A THESIS

Submitted to:

Oregon State University

in partial fulfillment of
the requirements for the
degree of

Master of Science

Presented October 2, 2015

Commencement June 2016

Master of Science thesis of Anthony L. Alberti presented on October 2, 2015

APPROVED:

Major Professor, representing Nuclear Engineering

Head of the School of Nuclear Science and Engineering

Dean of the Graduate School

I understand that my thesis will become part of the permanent collection of Oregon State University libraries. My signature below authorizes release of my thesis to any reader upon request.

Anthony L. Alberti

ACKNOWLEDGMENTS

I would like to take this opportunity to thank the individuals I have had throughout my life who helped me through trying times and encouraged me to press on. You helped shape me into the person I am today. And for that, I thank you.

I would also like to thank Dr. Javier Ortensi, Dr. Mark DeHart, and the rest of the reactor physics team at Idaho National Laboratory for their support in this work. Thank you for allowing me the opportunity to be a part of the TREAT project and I look forward to any future interactions we may have.

Dr. Todd Palmer. Thank you. Without your support and taking a chance on me coming out of my undergraduate studies, I would not be where I am today. I am honored to say that I am your student and am forever grateful. Here's to the past two years and to those ahead in what will be the roller coaster of a PhD.

Lastly, I would like to thank my parents for their undying support. You more than anyone know where my life has taken me, the experiences I have had, and those I have yet to have. I genuinely mean it when I say I could not have done this without you. I love you both. Thank you.

TABLE OF CONTENTS

TABLE OF CONTENTS (Continued)

LIST OF FIGURES

LIST OF TABLES

LIST OF TABLES (Continued)

1 Introduction

This chapter contains a discussion of the necessary background information for the remainder of this thesis and is organized as follows: Section 1.1 discusses the background on the need for transient testing, Section 1.2 discusses several reactor physics simulation packages, Section 1.3 details the TREAT facility, and Section 1.4 explicitly states the objectives of this research.

1.1 Transient Testing of Nuclear Fuels

1.1.1 Background

The primary mission of the Department of Energy Office of Nuclear Energy (DOE-NE) is to provide credible data that can be used to advance nuclear power as an economically competitive energy resource that satisfies the energy, environmental, and safety needs of the U.S. [5]. At the core of this mission is to fully understand the mechanisms behind the behavior of nuclear fuels in off-normal transient conditions. Transient testing of nuclear fuels involves subjecting fresh or pre-irradiated fuel and associated structural material specimens to intense high power bursts of radiation. Information gathered from these experiments is used to support the development of next generation reactor fuel designs, research efforts for future generation reactor designs and to maintain the sustainability of the existing fleet of nuclear power plants [30].

Transient testing was an essential aspect of nuclear fuels science during the late 1950s and through the next thirty-five years into the early 1990s. Research and development in this field thrived due to the industry's need to establish fuel performance for the upcoming light water reactor fleet [5]. However, once fuels performance was well-established, the need for transient testing ceased and was suspended in 1994 [6]. With the current desire to develop safer, more sustainable fuel cycles for future reactor systems, DOE-NE has identified the need to resume domestic transient testing [30].

1.1.2 Test Facility Capability Gap

Testing capability will be needed for all future fuel types including light water reactor (LWR), high temperature gas reactor (HTGR), and sodium-metal cooled fast reactor systems (SFR) [21]. These newer, more advanced reactor systems will likely require new fuel types. Full length, prototypic-scale fuel pins (or TRISO particles) must be tested in a controlled environment and extensively evaluated to understand how they behave in accident scenarios. This data is particularly scarce and highly valuable for future licensing [30]. In order to provide the most robust data, rapid, shaped power pulses and robust, high fidelity in-situ fuel motion monitoring systems are necessary.

Few transient testing facilities in the world have the desired short time-scale experimental imaging required for transient operations. Even fewer have line-of-site access to experimental specimens [21]. Line-of-sight (e.g. a hodoscope) is crucial to allow for visual data on pellet clad interactions in pin geometries or TRISO particle layer interactions. Of the test facilities that do not have these capabilities, deductions of the phenomenological states from post irradiation examinations (PIE) must be made. Though valuable, deductions are not ideal because they provide no data on fuel damage as a function of time, which is crucial to licensing of new fuels.

1.1.3 Considered Facilities and Alternatives

Assuming standard management and operational maintenance of the chosen facility, test capabilities should be designed for a 40-year life cycle and based in the U.S. to provide access, security, and control of DOE sponsored activites [30], [47]. The facility should have sufficient hot cell access nearby capable of receiving irradiated specimens for PIE. To ensure power levels are sufficient for temperature limited tests, the facility of choice should be able to pulse to a power of around 19 gigawatts (GW) [30]. The facility should be flexible enough to allow for experiments with but not be limited to: full- and half-sized fuel pins, fuel pin bundles, TRISO fuel particles, and other associated structural materials [30]. With these outlined needs, the DOE chose to consider three alternatives: 1) Transient Reactor Test Facility (TREAT), 2) Annular Core Research Reactor (ACRR), 3) No action.

Transient Reactor Test Facility (TREAT)

TREAT is an air cooled, graphite moderated pulse type reactor specifically built to conduct testing of prototypic-scale fuel pins and bundles in transient overpower tests [30]. TREAT is also the only existing alternative that has the capability to capture in-situ fuel motion [30]. The proximity of the facility to INL's Materials and Fuels Complex effectively eliminates the use of public roads in the transportation of experiments. TREAT was last operated in 1994 and has been in a standby state since then. If selected as the facility for transient test operations, the data acquisition system, reactor electronics, hodoscope, and other associated reactor systems will be considered for replacement or upgrading due to age and general advancements made in electronics.

Annular Core Research Reactor Facility (ACRR)

ACRR is a water cooled and moderated, pulse type reactor focused on supporting DOE National Nuclear Security Administration security and weapons research [47]. In the 1980s, ACRR was used for DOE-NE fuels research. Unlike TREAT, ACRR does not have a fuel motion monitoring system or the capability to receive, handle, and process irradiated experiments [21]. For transient testing to occur at the ACRR, the construction of a new hot cell for experiment assembly would be necessary. The construction of a post-irradiation capable hot cell would be cost prohibitive and experiments would thus need to be shipped to INL for PIE. This poses a transportation issue to due to the irradiated experiments and potentially failed fuel being transported over public roads and lands.

No Action

This alternative involves not restarting the TREAT facility and not modifying the ACRR [47]. Transient testing would be undertaken at existing domestic and international facilities. This has significant drawbacks in that transient tests would be completed without in-situ fuel motion monitoring using small-scale static capsule specimens [21]. Licensing and deployment of new fuels would be solely based on partially validated simulations and testing of small fuel fragments [21]. This alternative thus poses an increased risk as no new fuel has been licensed for U.S. deployment without thorough, prototypic scale testing.

Cost and Risk Analysis

A cost and risk analysis of the above options are provided in Appendix A.

1.2 Modeling and Simulation Capabilities

Modern day computing power and state of the art advanced modeling and simulation (M&S) have the potential to significantly impact transient testing at TREAT. In the past, total core power and energy release in a transient was known only to ±10% [13]. Multiple tests were needed to calibrate transients and obtain desired energy deposition in experiments. This led to long and expensive pre-experiment characterization. If a simulation capability was developed that accurately characterized the behavior of TREAT under transients, operational efficiency would increase thereby effectively reducing experiment operation costs.

The dynamics of a nuclear system such as TREAT can be modeled by the time-dependent Boltzmann transport equation [27].

$$\begin{aligned}\left[\frac{1}{v}\frac{\partial}{\partial t}+\hat{\Omega}\cdot\vec{\nabla}+\Sigma_t(\vec{r},E)\right]\psi(\vec{r},\hat{\Omega},E,t) = &\int dE'\int d\Omega'\Sigma_s(\vec{r},E'\rightarrow E,\hat{\Omega}'\cdot\hat{\Omega})\psi(\vec{r},\hat{\Omega},E,t)\\ &+\chi_p(E)\sum_i(1-\beta_i)\int dE'\nu\Sigma_{f,i}(\vec{r},E')\phi(\vec{r},E',t)\\ &+\sum_l\chi_l(E)\lambda_l C_l(\vec{r},t)+S(\vec{r},\hat{\Omega},E,t) \qquad (1.1)\end{aligned}$$

where:

ψ = angular flux ; Σ_t = macroscopic total cross section ;

Σ_s = macroscopic scattering cross section ; Σ_f = macroscopic fission cross section ;

ν = number of neutrons emitted per fission ; χ_p = energy spectrum of prompt neutrons

χ_l=energy spectrum for delayed neutron precursor group l ; S = external source ; v = neutron speed

β = delayed neutron fraction ; λ_i = decay constant for delayed neutron group i

C_i = precursor concentration for delayed neutron precursor group i ; $\vec{r}$=position

E = energy ; $\hat{\Omega}$=angle ; t=time

A brief background on several time dependent simulation codes that have been used for

research reactor analysis will now be briefly discussed.

1.2.1 Attila

Attila uses a steady state form of Equation 1.1:

$$\hat{\Omega}\cdot\vec{\nabla}+\Sigma_t(\vec{r},E)\psi(\vec{r},\hat{\Omega},E,t)=\int dE'\int d\Omega'\Sigma_s(\vec{r},E'\rightarrow E,\hat{\Omega}'\cdot\hat{\Omega})\psi(\vec{r},\hat{\Omega},E,t)$$
$$+\chi_p(E)\sum_i\int dE'\nu\Sigma_{f,i}(\vec{r},E')\phi(\vec{r},E',t) \quad (1.2)$$

Angular and spatial dependence are discretized using discrete-ordinates S_N discretization and linear discontinuous finite-element spatial differencing (LDFEM) [28]. Energy discretization is achieved using the multi-group method [22]. Material properties (i.e. cross sections) are weighted over a given energy range and assumed constant for specific spatial positions. The general solution technique utilized in Attila is source iteration. This method is well known to converge slowly in highly scattering media. To overcome this, a diffusion synthetic acceleration (DSA) algorithm is employed [28].

Although Attila was originally developed only for steady-state problems, Attila can be effectively coupled to FORNAX, a nuclear transmutation code written by Radion Technologies, for time-dependent calculations [28]. Flux distributions at specified time steps are calculated and then passed to FORNAX. FORNAX solves a set of fully coupled equations for the production, depletion, and decay of nuclides using an expansion approximation based on the Oak Ridge National Laboratory code, ORIGEN [29].

Attila's performance compared to reference MCNP and MCNPX solutions has been evaluated [29, 22]. K-eigenvalue calculations comparing a 3D Attila Model to that of an MCNP model for the Advanced Test Reactor (ATR) and INL have been completed. Attila calculated an eigenvalue larger than MCNP by 1357.98 pcm [29]. Depletion capabilities with Attila/FORNAX coupling were compared against that of MCNPX for the Godiva critical sphere and results showed a consistent under prediction of eigenvalue, depletion and transmutation, as well as power [29].

A feasibility study comparing Attila results to that of other stochastic and measured data for the Oregon State University TRIGA (OSTR) reactor has also been completed [22]. Attila flux distributions for various regions of the OSTR core varied from 2% and 6%. The largest overpredictions from Attila when compared to stochastic (MCNP) and experimental solutions

were found to be due to multigroup cross section data and group structure [22].

1.2.2 PARCS

The Purdue Advanced Reactor Core Simulator (PARCS) is a reactor kinetics simulation tool that solves the steady state and time-dependent multigroup neutron diffusion equation in 3-D Cartesian geometry [24]. PARCS utilizes a simplified P_N discretization form of Equations 1.1 and 1.2 to obtain transport-quality results. PARCS is conventionally a light water reactor (LWR) code and can be used as a standalone neutronics code or can be coupled to RELAP5 for thermal-hydraulic analysis [35]. Development of non-orthogonal mesh elements have also been developed allowing for the simulation of different fuel assembly types (e.g. VVER) [7].

PARCS utilizes finite difference methods for spatial discretization. Course mesh finite differencing is used for acceleration. Flexibility in time discretization schemes (explicit/implicit euler, Crank-Nicholson, etc) are allowed through the use of the theta-method [7].

PARCS coupling to RELAP5 for multiphysics kinetics simulations is completed through a message passing interface [24]. Temporal coupling between RELAP5 and PARCS is explicit and implemented in the following manner: The hydrodynamics code first calculates heat conduction solutions which are transfered to PARCS and thus incorporates appropriate feedback mechanisms into cross sections and flux distributions. Updated cross sections and flux distributions are used to recalculate the heat source which is then transferred back to RELAP5, ending a temporal time step [24]. This process is repeated until one of the codes sends a signal to terminate the calculation (user inputted or fault signal) [24].

Performance of PARCS as a standalone code as well as coupled to RELAP5 has been evaluated by Hamidouche, et al [16] for an idealized International Atomic Energy Agency (IAEA) generic 10 MW highly enriched Uranium (HEU) Material Test Reactor (MTR). This reactor is a light water, pool type reactor and has been used historically as an IAEA standard research reactor for safety analysis. For steady state calculations, PARCS over predicted reference MCNP multiplication factors by 374 pcm. However, similar asymmetrical power distributions were observed between steady state PARCS and MCNP calculations [16]. Coupled PARCS and RELAP performance was evaluated by Hamidouche, et al for the same MTR during a reactivity insertion accident [16]. Standalone RELAP5/Mod3.3 with the point kinetics module results were used as reference values. The coupled neutronics/thermal-hydraulics PARCS/RELAP5 code system

was shown to over-predict the reference calculations by 167.13%, 25.47%, and 8.99% for power, maximum cladding temperature, and maximum coolant temperature, respectivly [16].

1.2.3 TD-KENO

Time dependent KENO, or TD-KENO, is a simulation package that utilizes hybrid (coupled MC and deterministic) methods for solving Equation 1.1 [13]. A quasi-static, flux factorization method is used to separate the flux into the product of a space, energy, and angle dependent shape function that changes slowly in time and a time dependent amplitude function [12].

$$\psi(r, E, \Omega, t) = T(t) \cdot \phi(r, E, \Omega, t) \tag{1.3}$$

Equation 1.3 is then inserted into Equation 1.1 and after a number of algebraic manipulations, expressions for the shape and amplitude functions are obtained. Because the shape function typically is slowly varying in time, it is only numerically computed at infrequent time intervals. The more rapidly changing amplitude function (which is noticeably simpler than the shape function) is computed on small time intervals enabling accurate temporal solutions with decreased computational cost [12].

The flux shape, $\phi(r, E, \Omega, t)$, is found via KENO V.a, a 3D Monte Carlo reactor physics code within SCALE6.1 [14]. SCALE6.1 is a tool set from Oak Ridge National Lab for studying reactor criticality safety, reactor physics, spent fuel, radiation shielding, and uncertainty analysis [36]. Using this calcualted shape, kinetics parameters are calculated followed by solving the time dependent amplitude and precursor equations. This process is known as the improved quasistatic method [12].

Performance of TD-KENO has been evaluated based on a r-z geometry, delayed supercritical transient diffusion theory problem with two neutron energy groups and six delayed neutron groups [12]. It was shown that in this problem, calculated power relative to a reference transport solution showed good agreement at the onset of the transient. However, as the transient progressed, the calculated power deviated from the reference solution with a maximum difference of approximately 8% [12]. Normalized two-group flux distributions exhibited accurate behavior with the exception of a dip at the axial midpoint. This deviation was concluded to be due to a combination of inaccurate capture cross sections and transport effects [12].

1.2.4 PROTEUS

PROTEUS is the reactor physics toolset within SHARP (Simulation for High-efficiency Advanced Reactor Prototyping), the fast reactor core simulation suite from Argonne National Laboratory (ANL). PROTEUS is specifically developed for cross section generation, radiation transport, and fuel cycle modeling of fast reactors [1, 46]. The radiation transport module of PROTEUS has a finite volume and nodal diffusion solver as well as S_N and P_N discretization schemes for the second order form of Equation 1.1 [49]. The S_N discretization transport solver uses a continuous Galerkin finite element method in space, a multigroup approximation in energy, and a discrete ordinates scheme in angle [43]. These solvers are designed to use on the order of 100,000 processors or more for large, complex problems (i.e. increased heterogeneity) [49].

Cross sections within PROTEUS are computed from detailed, 3D, fine group spectrum calculations for specific compositions and temperatures with explicit representation of resonance structures using a method of characteristics (MOC) solver [49]. In order to minimize approximations, spectral calculations are completed using the multigroup P_1 equations for the entire energy range with an extended transport approximation up to the 9^{th} order [49]. Furthermore, isotropy approximations are removed by including anisotropic scattering matrices. This process results in fine group, region-wise or cell-averaged group cross sections [49].

Time dependence in PROTEUS-SN is incorporated through an adiabatic approximation and is solved through two sets of coupled equations [43]. The first set is identical to the point reactor kinetics equations with the expection that the kinetics parameters, $_\beta$ and ρ, are time depenedent. The second set is a transport like system for the shape function that includes the delayed neutron source and steady state transport solution 1.2 [43].

The following approximations are made in order to obtain the adiabatic approximation:

1. The time derivative of the shape function (i.e. angular flux) is negligible.
2. The shape function for the delayed neutron source is the same as the prompt source.
3. The time derivative of the magnitude function is negligible.

These reduce the shape equation to the steady state transport equation. This is then coupled with time-dependent kinetics parameters on the adjoint and forward fluxes and solved on each time step.

Performance of the S_N and P_N solvers in PROTEUS were evaluated based on an ANL Advanced Burner Test Reactor (ABTR) design [2]. Reference eigenvalue solutions produced in MCNP were found to be 1.01406±0.00004. For the P_N solver a spatial mesh resolution of 461,219 nodes with an angular discretization to the 9^{th} order was necessary for convergence of the eigenvalue and was found to be 55 pcm below that of the reference solution. A similar convergence study was completed for the S_N solver. The same 461,219 node model with an angular discretization of 98 angles was required for convergence. Subsequent calculations showed that fewer angles were able to be used but an increase in the mesh fidelity was required [49].

A separate benchmark study for the three transport models (S_N, P_N, and MOC) was completed for idealized thermal and fast reactors proposed by Takeda [45]. The thermal reactor benchmark was designed to be a Cartesian PWR-like design while the fast reactor benchmark was designed to be a medium-sized fast reactor with an assembly pitch of 12.99038 cm and a full 8 ring assembly [49]. Eigenvalue results compared to reference MCNP calculations are shown in Tables 1.1 and 1.2.

Solver	Eigenvalue	Difference (pcm)
MCNP	0.97760	72.249 (stat. uncert.)
P_N	0.97649	-116.277
S_N	0.97717	71.264
MOC	0.97686	-32.478

Table 1.1: Transport results for thermal reactor benchmark.

Solver	Eigenvalue	Difference (pcm)
MCNP	1.09515	33.363 (stat. uncert.)
P_N	1.09599	69.984
S_N	1.09494	-86.500
MOC	1.09353	-117.76

Table 1.2: Transport results for fast reactor benchmark.

1.2.5 MAMMOTH

MAMMOTH is the reactor physics package within the Multiphysics Object Oriented Simulation Environment (MOOSE) framework. MOOSE is a parallel, FEM framework specifically designed to solve systems of non-linear, coupled partial differential equations [48]. MAMMOTH inherits all of the MOOSE finite element functionality and is able to leverage a number of different physics applications to solve a variety of complex coupled reactor physics problems. This is completed by solving a large system of nonlinear equations on the same mesh input and solved implicitly using the Jacobian-Free Newton-Krylov (JFNK) method [10]. However, because solutions are required on a variety of time scales, implicit coupling is not optimal. Instead, a split operator approach is available allowing for each sub-application to solve respective physics and share a single mesh file [11].

A key feature of MAMMOTH is the architecture of the executable. MAMMOTH is compiled as a single executable code containing the executable libraries of each sub application [39]. Communication between the packages involves the MOOSE MultiApp system [11].

Sub-applications within MAMMOTH include Rattlesnake for neutron transport, BISON for fuels performance analysis, and RELAP-7 for low-resolution thermal fluids simulations [39]. The coupling of these physics packages has been evaluated for Rattlesnake and BISON [11]. In this work, a single fuel pin calculation was completed to investigate MAMMOTH's capability to capture detailed physics of plutonium buildup around the rim of a thermal reactor fuel pin as a function of time. Table 1.3 shows calculated eigenvalues for various order of angular refinement for a fuel pin temperature of 1000 K.

Solver	Eigenvalue	Difference (pcm)
SERPENT	1.29753	N/A
S_2	1.29753	246.691
S_4	1.29387	28.683
S_8	1.29234	-62.818
S_12	1.29237	-61.022

Table 1.3: MAMMOTH calculated eigenvalue results using discrete-ordinates, S_N discretization.

Multiphysics calculations were demonstrated by coupling two separate physics moduels: Rattlesnake for neutron transport and BISON for fuels performance. "Two-way" calculations were

performed by having power density and burnup values passed from Rattlesnake to BISON and correlating fuel temperatures passed back to Rattlesnake. Figures 8a and 8b in [11] show that calculated power densities and fuel temperatures are under-predicted in the center of the fuel pin and slightly over-predicted at the edge of the pin.

1.3 TREAT Facility

1.3.1 History and Background

The Transient Reactor Test Facility (TREAT) is a versatile test facility designed to physically evaluate nuclear fuels and associated structural materials in a variety of excursion scenarios. TREAT is located at the Materials and Fuels Complex (MFC) at Idaho National Laboratory (INL) (Figure 1.1). It was constructed in 1958 and first went critical in 1959. The facility conducted thousands of successful experiments until 1994 when operations were suspended [6]. Historically, the objective of TREAT was to provide quantitative data and visual information on the mechanisms involved with melting of fast reactor fuels and structural materials [9]. Experiments were expanded to include light water reactor (LWR) fuels and structural materials.

Figure 1.1: TREAT at MFC.

The TREAT core is a thermal spectrum, once-through, air cooled, heterogeneous system fueled by highly enriched uranium (HEU) dispersed in a graphite matrix. The uranium is in U_3O_8 form, is enriched to 93.1% U^{235}, and is mixed at a 10,000:1 Carbon to U^{235} ratio. Due to the dry nature of the reactor, a neutron radiography station and an experimental specimen line-of-site hodoscope can be employed for fuel motion monitoring (Figure 1.2).

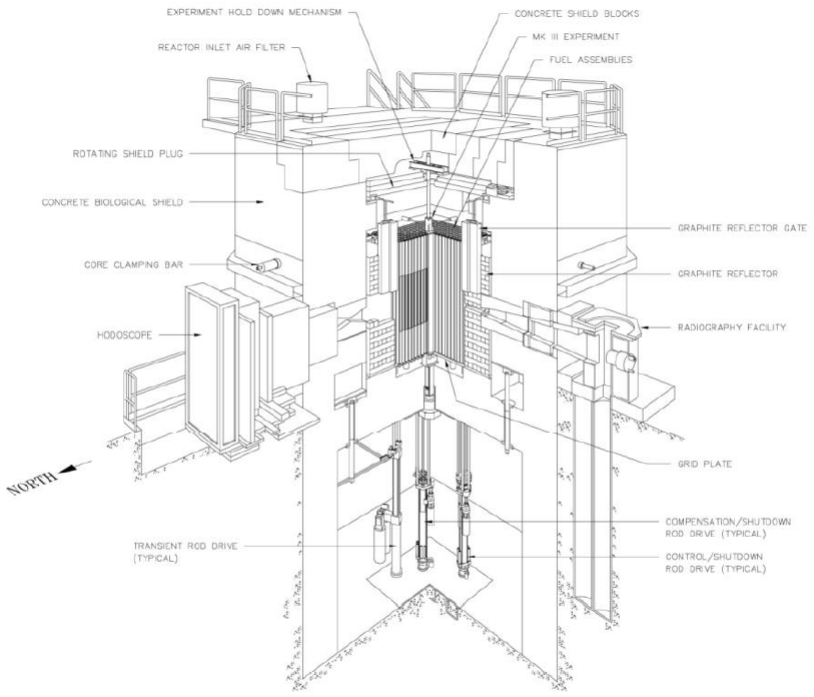

Figure 3: TREAT Schematic [7]

Figure 1.2: Cutaway view of TREAT.

The reactor operates at a steady state power of 100 kWth and can pulse up to 18,000 MWth. Safe operation of the reactor is based on the inherent negative temperature coefficient of the reactor core. In using graphite as the inert matrix for the fuel as well as the reflector material, the large relative mass of graphite compared to that of HEU acts as a heat sink for reactivity insertions. The majority of the heat is absorbed in the graphite and results in an increase in the overall bulk graphite temperature. This in turn causes an increase in thermal-upscattering of neutrons, spectral hardening, and increased neutron leakage out of the core. These combined effects lead to a subsequent decrease in reactivity and the safe inherent shut down of the reactor.

Assembly Types

The driver fuel is a four foot section of 4"x4"x8" active fuel blocks clad in zirconium-3 (Figure 1.3). On the top and bottom of the active fuel region are axial reflector assemblies comprised of graphite which are clad in 6063-aluminum two feet in length. In between the axial reflectors and active fuel are $\frac{1}{4}$" zirconium-3 spacers [9]. These spacers serve to delay heat transfer between

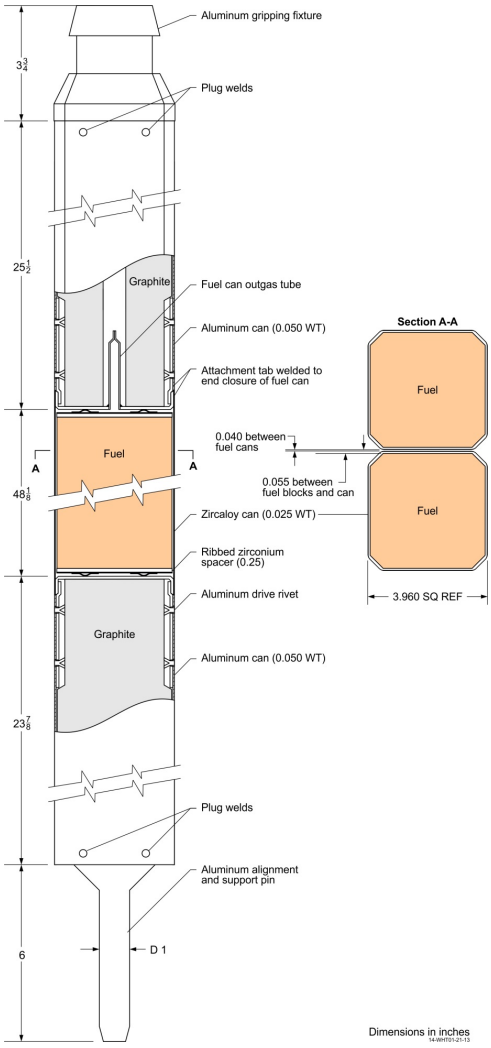

Figure 1.3: TREAT driver fuel.

the fuel and the aluminum clad of the reflector sections during severe transients [9].

In addition to the standard fuel assembly, there are a number of special-purpose assemblies throughout the core. To maintain core configuration flexibility, they are geometrically similar to the standard fuel assembly (Figure 1.4).

Control elements are identical to fuel elements except for a 1.875" outer radius zircaloy-2 tube that contains a carbon steel tube packed with B_4C powder [23]. These elements are separated into three banks: 4 compensation rods, 8 control/shutdown rods, and 4 transient rods. The role of each bank is as follows: compensation rods are used to maintain reactivity levels during transients, control/shutdown rods are used to end a transient and shutdown the reactor, and the transient rods are used to initiate transient operations.

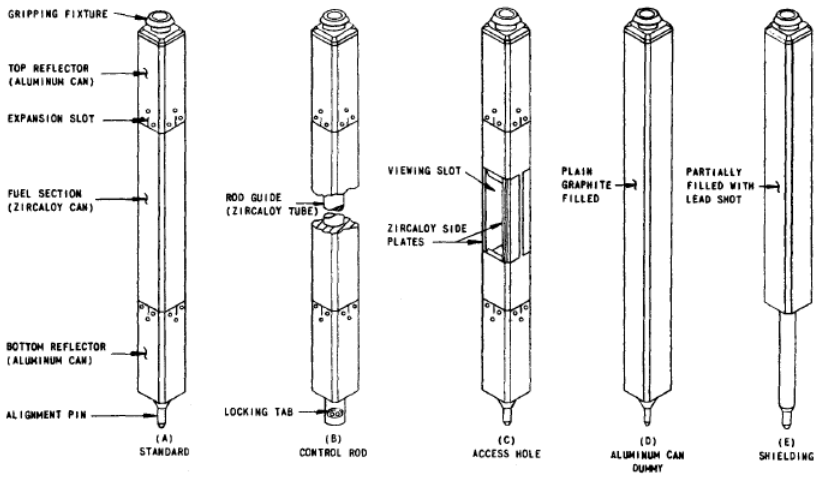

Figure 1.4: Standard and special assemblies for TREAT core.

Access hole assemblies may either be fuel or reflector assemblies with the central two foot section removed and voided [23]. This void serves as an access port for the fuel motion monitoring systems.

Graphite and lead shot filled dummy assemblies are identical to fuel elements geometrically but serve as radial reflector and shielding assemblies, respectively.

1.3.2 Physics of TREAT

Graphite moderated reactors exhibit characteristics different than that of other reactor types. Table 1.4 shows a comparison of select neutron physics parameters for a variety of reactor types.

Reactor Type	Ave. Diffusion Length (cm), L_{th}	Fermi Age-to-Indium, τ_{in}	RMS Dist. to capture from birth (cm), $\langle r_{abs} \rangle$	Num. of Collisions to thermal
PWR	1.8*	40*	16.1	16*
HTGR	12*	300*	51.6	43*
TREAT	22	540^{+}	76.4	97

Table 1.4: Select fast spectrum neutronics parameters comparing TREAT to other common reactor types. Pressurized water reactor (PWR) is water moderated; High Temperature Graphite Reactor (HTGR) is graphite moderated. *[8], $^{+}$[37].

The average number of collisions to thermalize is based upon the following formula [8]:

$$< \# >= \frac{u}{\xi} = \frac{\ln \frac{E_0}{E}}{1 + \frac{\alpha}{1-\alpha} \ln(\alpha)} \tag{1.4}$$

where:

$E_0 = 2MeV$ & $E = 1eV$

α is known as the collision parameter and is defined as [26]:

$$\left(\frac{A-1}{A+1}\right)^2$$

The root mean square distance to capture from birth, $\langle r_{abs} \rangle$, is calculated based on the fundamental definition of the migration area, M^2_{abs} [8, 25]:

$$M^2_{abs} = L^2_{th} + \tau_{in} \tag{1.5}$$

$$\left(\frac{1}{\sqrt{6}} \langle r_{abs} \rangle\right)^2 = \left(\frac{1}{\sqrt{6}} \langle r_{th} \rangle\right)^2 + \left(\frac{1}{6} \langle r^2_{in} \rangle\right) \tag{1.6}$$

$$\langle r_{abs} \rangle = \sqrt{\langle r^2_{th} \rangle + \langle r^2_{in} \rangle} \tag{1.7}$$

where:

r_{th} = root mean squre, crow flight distance from where a neutron enters the system at a thermal energy to where it is captured [25].

r_{in} = root mean squre, crow flight distance from where a neutron is born in fission to where it slows to thermal energies [8]. r_{abs} = root mean squre, crow flight distance from where a neutron is born in fission to where it is captured as a thermal neutron [8].

The increased diffusive behavior of TREAT over that of other more common reactor types is observed though the increase in number of collisions to thermalize and the RMS distance to capture from birth. This diffusivity is an important factor in accurately modeling TREAT operations.

Figure 1.5 shows a typical Maxwellian neutron spectrum at 300 K and 600 K. As the fuel temperature in TREAT increases, there is a shift (known as "hardening") in the spectrum away from the 1/v cross section region leading to a reduction in reaction (i.e. fission) rates. This reduction in fission leads to an increased neutron population outside of the fuel and in the

reflector. During transient operations, the high specific heat of graphite causes the reflector to be physically cooler than that of the fuel, remain at the "softer" 300 K spectrum, and maintain elevated reaction rates. This phenomena is confirmed by the results shown in Table 1.5.

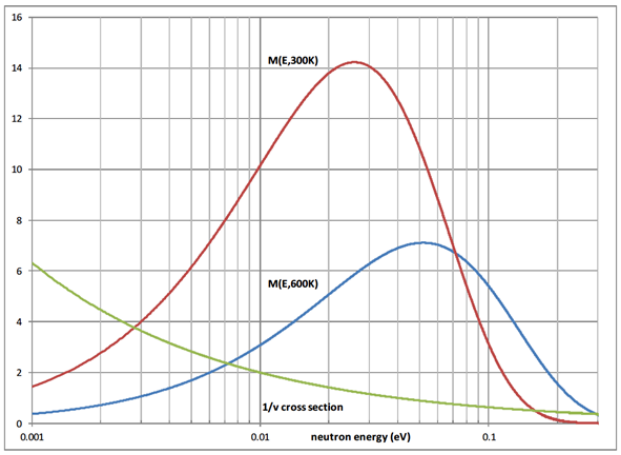

Figure 1.5: Standard Maxwellian distribution at 300K and 600K.

Fuel Temp [K]	% System Leakage	% System Capture	% Fission
300	8.9	49.5	41.6
600	10.2	55.1	34.7

Table 1.5: Increased leakage and capture reactions are driven by the cooler reflector graphite while decreased fission reactions are driven by the hotter fuel.

1.4 Research Objectives

The purpose of this work is to develop a steady state, full core neutronics model of TREAT using MAMMOTH and to use this model to:

1. Identify fundamental neutronics properties.
2. Quantify the effects of spatial homogenization and angular discretization on:
   - Power Distribution
   - Eigenvalue
   - Reaction Rates: Fission source, capture, and leakage rates.

3. Establish functional treatment of diffusion coefficients in highly anisotropic regions such as cooling channels.

4. Provide accurate base model for transient modeling.

In order to complete the above objectives, analyses of single assembly calculations were initially completed followed by full core calcualtions. Neutronic performance and accuracy of developed deterministic models will be based on comparisons to reference Monte Carlo (SERPENT 2) solutions.

2 Methods and Modeling Approach

Due to inconsistent historical experimental data of the TREAT facility for the minimum critical core configuration, calculated results from MAMMOTH were verified against reference Monte Carlo based solutions from SERPENT. To enhance continuity between these two code suites, cross section data used in MAMMOTH was calculated by SERPENT from reference solutions.

The following sections of this report will describe the specific tools and how they were used in this work. Section 2.1 will discuss SERPENT and how it was used to generate cross sections for MAMMOTH; Section 2.2 will discuss CUBIT and the methods used to create the finite element geometries and mesh; and Section 2.3 will discuss MAMMOTH and the homogenization techniques used in this work.

2.1 Nuclear Data Preparation

Cross sections used in this work were calculated primarily from SERPENT 2, a Monte Carlo reactor physics analysis code developed at VTT Technical Research Centre of Finland [42]. SERPENT 2 was chosen based on: 1) its capacity for full 3D simulations; 2) spatial homogenization; and 3) group constant generation for deterministic calculations [42]. In this work, the continuous energy ENDF/B-VII.r1 library was used. Homogenized group wise data is calculated using a flux and volume weighted formulation (Equation 2.1).

$$\Sigma_{x,i}^{g} = \frac{\int_{D_i} \int_{E_{g-1}}^{E_g} \phi\left(r,E\right) \Sigma_x\left(r,E\right) dE dV_i}{\int_{D_i} \int_{E_{g-1}}^{E_g} \phi\left(r,E\right) dE dV_i} \tag{2.1}$$

Deterministic neutron transport codes, such as those found within the SCALE package, generate cross sections based on 2D lattice based transport calculations [3]. Table 2.1 shows evidence as to why this method is unsuitable for TREAT analysis and that cross section generation based on 3D simulations is required.

In Table 2.1, various key neutronics parameters are shown for three different models. The first model, *TREAT Fuel*, is a 2D slice of the TREAT fuel surrounded by reflecting boundary conditions creating an infinite lattice. This is the traditional approach used for cross section development in the power reactor community. The following two models are three dimensional

Parameter	TREAT Fuel	TREAT Assembly	TREAT Full Core
Ave. Num. of Collisions to Thermal	94.60	96.75	96.89
Ave. Num. of Collision While Thermal	47.96	62.88	95.79
Dist. Traveled to Thermal Energy (cm)	48.04	53.72	52.59
Dist. Traveled While Thermal (cm)	48.51	54.70	55.39
% Elastic Scattering Reactions	55.86	52.48	40.48
% Bound Scattering Reactions	43.39	56.88	59.08

Table 2.1: Neutronic parameters based on input geometry from reference SERPENT 2 calculations. Bound scattering is defined as the sum of incoherent inelastic and coherent elastic scattering reactions occurring at thermal energies.

models that increase in complexity. The *TREAT Assembly* model is a single fuel assembly (see Figure 1.3) with radial reflecting boundary conditions and extrapolated zero-flux boundary conditions on top and bottom. The *TREAT Full Core* is a full core model with extrapolated zero-flux boundary conditions on all exterior surfaces. Table 2.1 shows that as models increase in complexity, slowing down and scattering parameters change. For example, in comparing the average number of collisions while thermal, the 3D assembly and core models increase by 31.1% and 99.73% over that of the 2D fuel slice. This shows the diffuse character of the TREAT core and the fact that many neutrons leave the core, thermalize, and scatter outside of the core in the reflectors before returning to the core where they are absorbed. Furthermore, the % elastic and bound scattering reactions decrease and increase respectively with increasing model complexity because of the inherent scattering physics of graphite. In the assembly and core models, there are increasing amounts of non-fueled graphite in which neutrons thermalize. It has been shown [50, 15] that when neutron energies are sufficiently low, the wavelength of neutrons becomes sufficiently large that coherent elastic scattering is not possible and only inelastic scattering is possible.

2.1.1 Group Structure

Based on previous High Temperature Reactor (HTR) studies, 26, 14, 11, and 8 neutron energy group structures were evaluated [20]. The 14- and 11-group structures are derived from the 26-

group structure by merging the higher energy groups and maintaining low energy group fidelity. The 8-group structure was from a separate HTR study. In addition, an equal lethargy bin 10-group structure was evaluated. This particular structure is based on the fact that the TREAT core consists primarily of graphite and that the total cross section for graphite is well-behaved and resonance free [34]. Figure 2.2 shows the error in calculated power from MAMMOTH for a half assembly model (shown by Figure 2.1) for the various group structures.

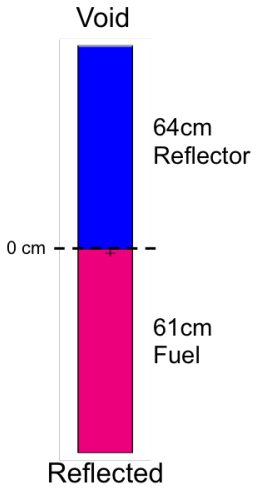

Figure 2.1: Half assembly model used for group structure and spectral flux analysis.

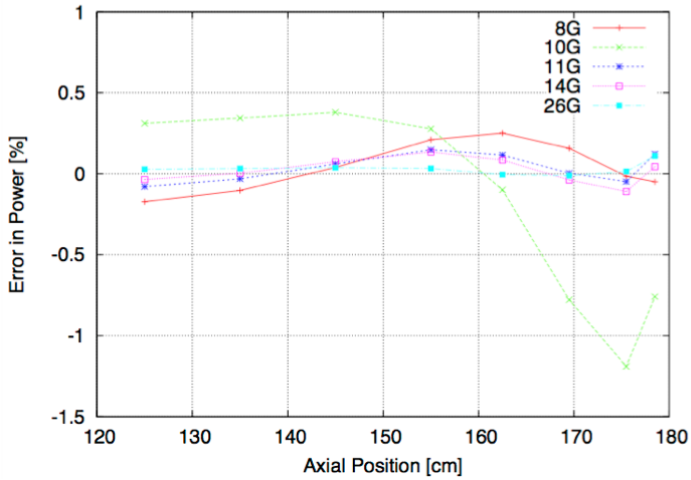

Figure 2.2: Energy group structure evaluation results.

The 26-group structure produces the lowest error while the equal spaced lethargy 10 group structure produces the highest error. Since the 11- and 14-group structure give a similar error distribution the 11-group structure was chosen in order to reduce computational expense.

2.1.2 Axial Cross Section Region Refinement

Previously studied graphite reactor analysis shows strong fuel-reflector interface effects which create large spatial flux gradients [20]. Furthermore, it has also been shown that inaccuracies increase in flux weighted cross sections when weighted over large flux gradients [17]. In order to develop more accurate axial cross section regions, a spatial-spectral analysis was completed using the half assembly model shown in Figure 2.1. SERPENT 2 flux tallies were placed at various locations allowing for a spatial analysis of the flux distribution (Figures 2.3 and 2.4).

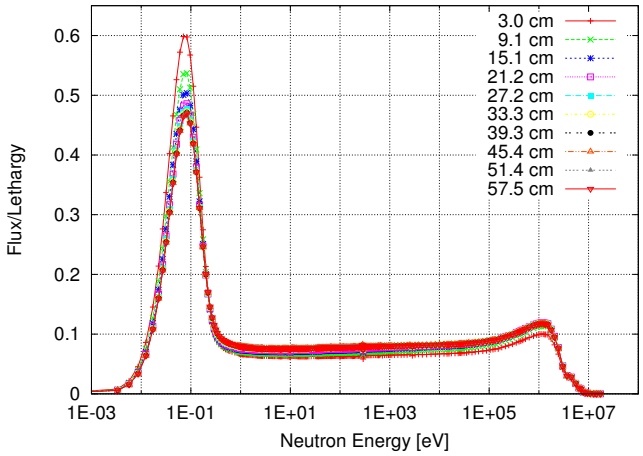

Figure 2.3: Flux spectra in active fuel.

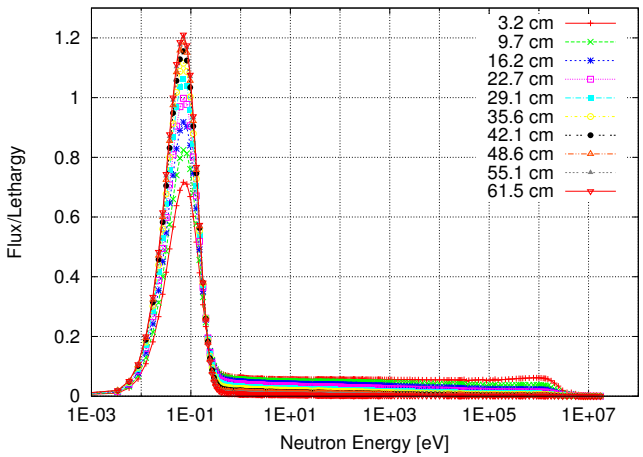

Figure 2.4: Flux spectra in axial reflectors.

Material regions where gradients in the flux were small were given a single cross section region. This can be seen in Figure 2.3 above 20 cm. For axial positions less than 20 cm, i.e.

closer to the reflector interface, Figure 2.3 shows large flux gradients in the 0.01 eV to 1 eV (thermal energy) range. This led to the fuel region being split into two separate sections, a 20 cm region closest to the interface and a central 80.97 cm region.

Figure 2.4 shows a more continuous flux gradient than that of Figure 2.3 because the reflector is a source free, scattering dominated medium. With this more continuous spectral effect, the reflector was split into three separate regions, a 10.48 cm region nearest the interface, a 25.23 cm region in the center, and a 27 cm region towards the outer periphery.

2.1.3 Diffusion Coefficient Generation

A drawback of using SERPENT 2 for cross section generation is the fact that SERPENT cannot compute accurate diffusion coefficients for near-void regions because it uses a transport corrected total cross section (Equation 2.2).

$$D = \frac{1}{3\Sigma_{tr}} = \frac{1}{3\left(\Sigma_t - \Sigma_{s1}\right)} = \frac{1}{3\left(\Sigma_t - \bar{\mu}\Sigma_{s0}\right)} \tag{2.2}$$

In near void regions, the average cosine of the scattering angle, $\bar{\mu}$, and total cross section, Σ_t are near zero. Because of this, the denominator of Equation 2.2 approaches zero and forces the calculated diffusion coefficient to increase to non-physically large values.

Because of these difficulties in SERPENT, diffusion coefficients for near void regions in this work are calculated by DRAGON-5, which uses a diffusion-like tracking method [32]. This method uses a standard collision probability technique and infinite cell collision probablity method where the media of interest is folded into an infinite 2D lattice [31]. Furthermore, DRAGON has the capability to calculate coefficients based on a P_0, P_1, B_0, B_1, or transport-corrected B0 model [32]. For this work, the B_1 model was used. The importance of the diffusion coefficient and its effect on simulation results will be discussed in subsequent sections of this thesis.

2.2 Mesh Preparation

Geometric models and their corresponding meshes are created with CUBIT, a mesh generation toolkit designed by Sandia National Laboratory [33]. CUBIT was designed to create either

structured or unstructured mesh elements in two- and three-dimensions [33] and was initially built to generate quadrilateral and hexahedral meshes but has been expanded upon to include triangular and tetrahedral mesh elements [33].

Finite element models are created in the EXODUS-II format. This format is used for efficient data storage and allows for problem definition, visualization and data extraction, and code-to-code data transfer within a singular mesh file [40]. Because of this capability, models for reactor analysis in MAMMOTH simulations use a single mesh file.

In all of the models analyzed, two first-order mesh element types are used, hexahedral and wedge. Figures 2.5 and 2.6 show each of these elements, respectively.

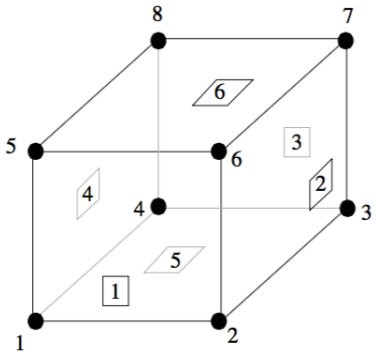

Figure 2.5: General first order, 8 node, hexahedral element. Each node and surface are numbered respectively.

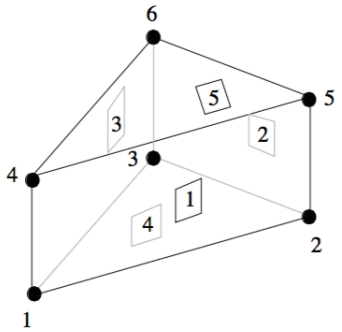

Figure 2.6: General first order, 6 node, wedge element. Each node and surface are numbered respectively.

Material properties and boundary conditions are applied to models via grouping of mesh elements. Elements of the same type are be grouped together and assigned material properties (i.e. cross sections). Though this process is relatively efficient, element blocks cannot have more than one mesh element type [40]. Boundary conditions are applied by grouping particular faces or edges into side sets. Though element blocks and sidesets can be comprised of the same elements, they are completely independent of one another.

Mesh continuity between surfaces and volumes is an important facet of radiation transport and is maintained in CUBIT through joining adjacent like surfaces together to form a singular surface. For this to occur, adjacent surfaces must have like topology and geometry. This is ensured by "imprinting" adjacent curves, vertices, and surfaces with one another. Once all adjacent geometric entities are imprinted, they are merged together to form a singular surface. Within CUBIT, this process is known as an "imprint and merge".

2.2.1 CUBIT Scripting for Efficient Model Development

A Python interface is built into CUBIT allowing geometrical bodies and their associated meshes to be created and stored. It also provides an object-oriented structure that gives users the ability to easily manipulate and query bodies. Because of these scripting capabilities, the flexibility of mesh element usage, material property assignment, and boundary condition assignment, CUBIT is often used as the mesh generation tool for MAMMOTH applications.

Models analyzed in this report utilized the Python interface within Cubit and were created using a modular format. The following general module format was used: 1) main input; 2) geometry building functions; 3) advanced CUBIT functions; 4) main executioner. The main input is used to store model specifications such as mesh refinement, geometrical dimensions, and domain identifiers for material property and boundary condition applications. Due to the similarity of each of the elements in the TREAT core, it was possible to create the general geometrical shapes used in the models via general geometry building functions. These functions were stored as a separate module script for ease of editing and modifying models. The advanced function module allows users to call predefined functions that query and manipulate geometrical objects. The executioner is the main file that links the other three modules to create, modify, and mesh the models.

3D models were made in the following order with their corresponding parent Python module(s) enclosed in square brackets:

1. Build assemblies to exact dimensions [1,2].
2. If core configuration, arrange assemblies via core map [1,4].
3. “Imprint and merge” [4].
4. Specify mesh interval refinement and mesh schemes [1,3,4].
5. Mesh top-most surfaces of geometries with 2D mesh [1,3,4].
6. Sweep and extrude top surface mesh through rest of respective volume to produce 3D mesh [3,4].
7. Group like elements into blocks for efficient material property application [1,4].
8. Group outer-most surface elements into sidesets for boundary condition application [3,4].
9. Export complete model [4].

2.3 MAMMOTH Models

To ensure the accuracy of the other coupled physics modules within MAMMOTH, it is imperative to be able to solve the steady state power distribution within TREAT. This is done through eigenvalue calculations in Rattlesnake.

2.3.1 Neutron Transport within MAMMOTH - Rattlesnake

Rattlesnake is the radiation transport solver within MAMMOTH and has the following capabilities:

1. Solving transient and eigenvalue problems for models in one, two, or three dimensions.
2. A general treatment of anisotropic scattering via Legendre expansion in the scattering cosine.
3. Multigroup diffusion.
4. Second order self-adjoint angular flux (SAAF) transport formulations.
    - S_N and P_N discretizations.
5. Multigroup interpolation and mixing operations.
6. Control Rod movement, feedback, depletion, criticality search, etc.
7. Nonlinear Diffusion Acceleration (NDA).

In this work, eigenvalue problems are solved with both multigroup diffusion theory and the P_N discretization of the SAAF formulation of Equation 1.1. In the P_N discretization calculations, first order anisotropic scattering was utilized.

2.3.2 Homogenization Technique

In the second order SAAF transport formulation, there is a $\frac{1}{\sigma_t}$ dependence that causes numerical instabilities in near-void regions - e.g. the air cooling channels and interassembly gaps in TREAT. These instabilities were alleviated through the removal of near-void regions through homogenization.

The basic idea of homogenization is to reduce computational cost by avoiding the explicit modeling of highly heterogeneous media and to create simplified, homogenized regions [44]. In this process it is important to maintain specific reactor properties such as eigenvalue, reaction

rates, and power densities [44]. Furthermore, as one adds complexity to homogenized models and approaches the fully heterogeneous or reference model, one should observe marked improvements in the preservation of these parameters. Using this general approach to remove near void regions, the following homogenizations were utilized for this work:

1. Full radial homogenization
    - All radial volumes are smeared into a single volume.
2. Full main homogenization with explicit cooling channels and interassembly gaps.
    - Main, clad gap, and clad are smeared into a single volume.
    - Cooling channels and interassembly gaps are explicitely modeled.
3. Clad gap, clad, cooling channel, and interassembly gap homogenization.
    - Main is left explicitly modeled.
4. Clad gap and clad homogenization.
    - Main, cooling channels, and interassembly gaps are explicitly modeled.
5. Full heterogeneous.

In the above descriptions, "main" is a general term that is axial position dependent and refers to either the fuel or reflector blocks (see Figure 1.3).

2.3.3 Standard Assemblies

Standard assemblies include fuel, zirconium-clad reflector, and aluminum-clad reflector assemblies. Each of these are geometrically identical and only differ in the materials that comprise them. Figures 2.7 to 2.11 show a top down view of the radial meshing used in each of the homogenization schemes. Figure 2.12 shows the standard axial mesh refinement used for all models in this work. In Figure 2.7, only first-order hexahedral mesh elements were used. In Figures 2.8 to 2.11 first order hexahedral and wedge elements were used.

For single fuel assembly, infinite lattice calculations, reflective boundary conditions were applied on each radial surface and an extrapolated zero-flux condition was applied on the top and bottom.

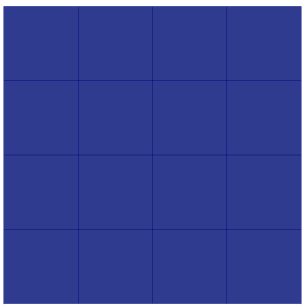

Figure 2.7: Top down view of full radial homogenization scheme.

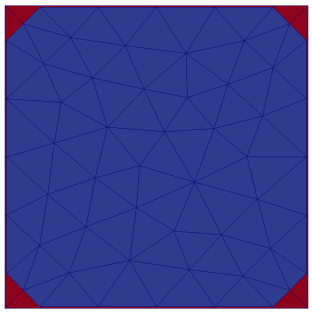

Figure 2.8: Top down view of full main homogenization with explicit channels and interassembly gaps scheme.

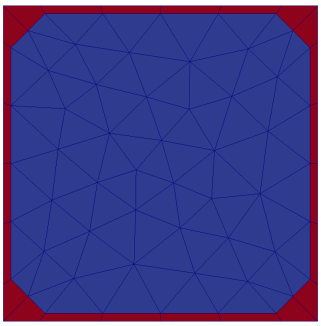

Figure 2.9: Top down view of clad gap, clad, cooling channels, and interassembly gap homogenization scheme.

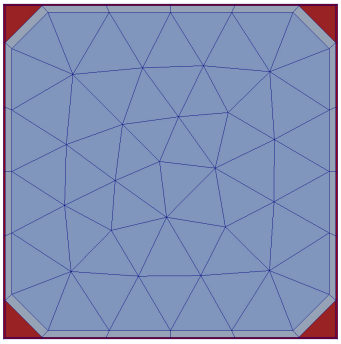

Figure 2.10: Top down view of clad gap and clad homogenization scheme.

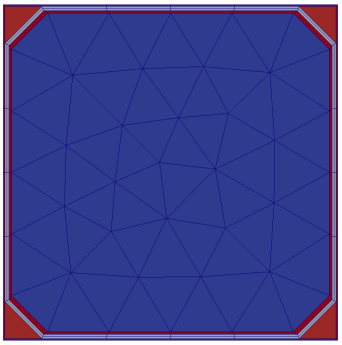

Figure 2.11: Top down view of radial heterogeneity scheme.

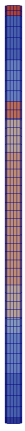

Figure 2.12: Side view of standard axial mesh fidelity.

2.3.4 Control Assemblies

Control assemblies within TREAT are manufactured by boring out a 2.54 cm cylindrical tube out of the center of the fueled portion of the standard fuel assembly. A 2.22 cm B_4C poison rod and 0.3175 cm thick cladding comprise this bored out region (Figure 2.13). However, for the purposes of this research, the B_4C poison rod and associated clad were smeared into the rest of the assembly and can be represented by a standard assembly type. This homogenization was selected for simplicity as well as due to the fact that diffusion theory fails in highly absorbing media. Future work will include more sophisticated control assembly modeling.

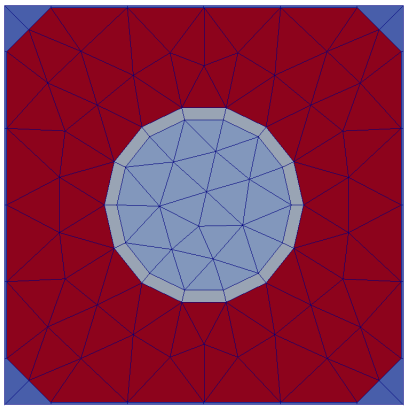

Figure 2.13: Top down view of control rod configuration within full homogeneous with explicit channels fuel modeling scheme.

2.3.5 Minimum Critical Core

The core configuration for the minimum critical core is shown in Figure 2.14. It consists of 138 fuel assemblies, 8 control assemblies, 40 zirconium-clad reflector assemblies, and 175 aluminum-clad reflector assemblies. Furthermore, the minimum critical core is surrounded by a permanent reflector of two radial feet of Chicago-Pile 2 (CP-2) graphite. Between this permanent reflector and the 19x19 main core is a 2" air gap. Because of this gap, the clad gap, clad, cooling channel, and interassembly gap model (homogenization #3) was not considered for full core use. This specific homogenization was developed for the SAAF formulation solver within Rattlesnake and the air gap presented a near-void region that introduced numerical instabilities. Furthermore,

results for the clad gap and clad homogenization produced unacceptably large errors and were therefore removed from this work. For the models tested, extrapolated zero-flux boundary conditions were applied to each exterior surface.

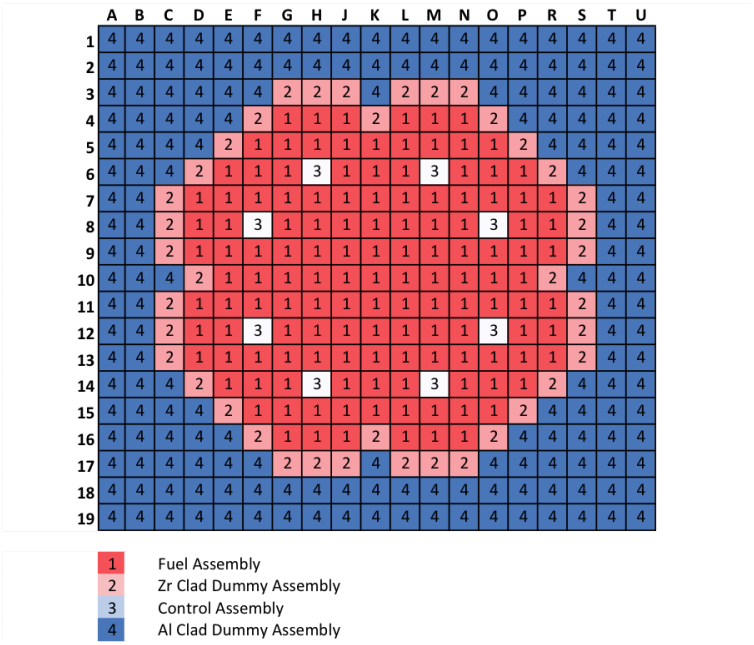

Figure 2.14: Minimum critical core configuration.

Figure 2.15 shows a one-quarter top down view of the meshed core with full radial homogenization. In this scheme only first order hexahedral elements were used. Figure 2.16 shows a one-quarter top down view of the meshed core with full main homogenization with explicit cooling channels and interassembly gaps. This model and the heterogeneous model used first order hexahedral and wedge elements.

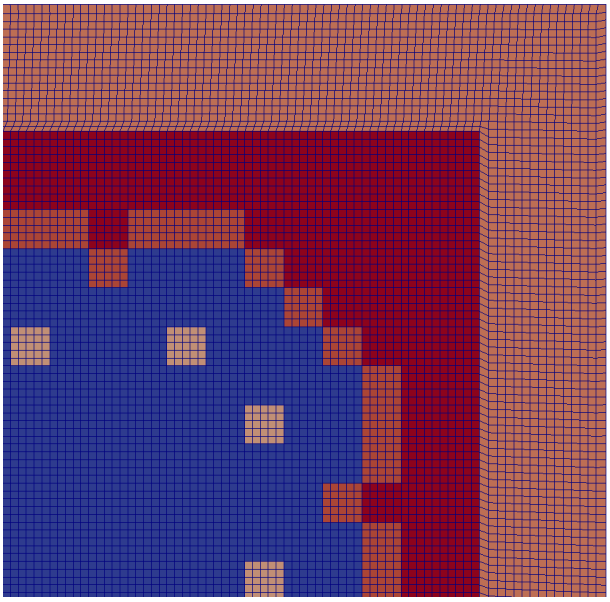

Figure 2.15: Full radial homogenization for minimum critical core configuration.

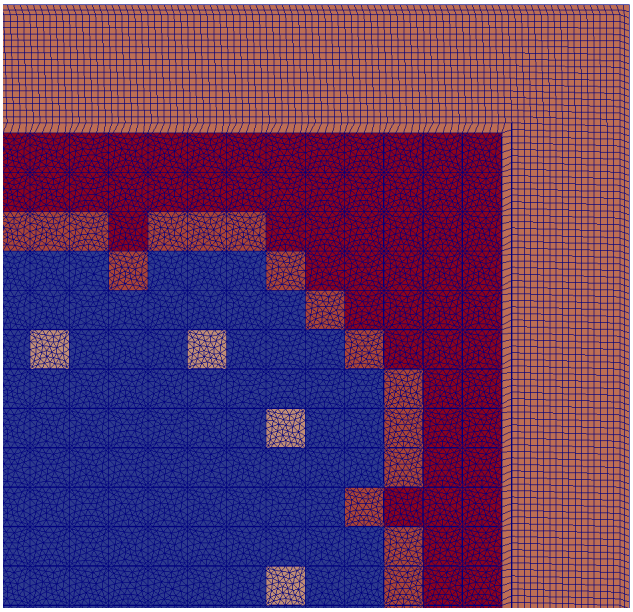

Figure 2.16: Full fuel homogenization with explicit interassembly gap and channel model.

3 Results

Solutions for all models will be generated from diffusion theory calculations. Those models without near void regions will also be computed using low and high order, discretized P_N transport. Assembly models will be evaluated on axial power distributions, k_{eff}, and integral reaction rates. Full core models will involve computation of the following: 1) axially integrated, radial power distributions; 2) radially averaged, axial power distributions; 3) k_{eff}; and 4) integral reaction rates. All simulations are normalized to an arbitrary power of 2000W.

It is important to note that the value of k_{eff} is a balance between the production, absorption, and leakage rates (Equation 3.1).

$$k_{eff} = \frac{production\,rate}{leakage\,rate + absorption\,rate} \tag{3.1}$$

Since k_{eff} is an integral parameter, it is difficult to determine the extent of cancellation of error between over prediction and under prediction of respective reaction rates when compared to reference results. Therefore it is also necessary to compute specific integral reaction rates (i.e. fission source, capture, and leakage rates).

All reference solutions were run with one million source neutrons per cycle. The number of inactive cycles necessary for convergence of the fission source was determined by calculating the Shannon entropy based on source points and source weight [38]. A total of 10 inactive cycles was determined to be necessary for the convergence of all of the target temperatures. Because SERPENT does not use any type of variance reduction, 1,000 and 3,000 active cycles were required for the single assembly and full core calculations, respectively [38].

3.1 Single Assembly, Infinite Lattice Calculations

Reference reaction rates for the single assembly are shown in Table 3.1. Sections 3.1.1, 3.1.2, 3.1.3, 3.1.4, and 3.1.5 discuss calculated results from MAMMOTH for each of the homogenization models.

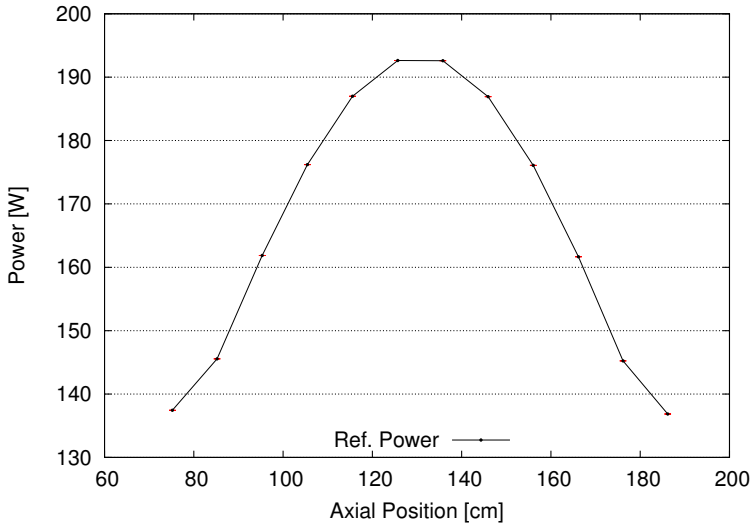

Figure 3.1: Reference power shape for single fuel assembly. APD error bars are shown in red.

Temp [K]	k_{eff} (pcm)	Fission Source Rate	Capture Rate	Leakage Rate
293	1.42154 (1.50)	1.05962E+14	4.04515E+13	3.69841E+12
400	1.40577 (1.60)	1.07147E+14	4.14600E+13	3.87904E+12
600	1.37909 (1.60)	1.09229E+14	4.32247E+13	4.18763E+12
800	1.35715 (1.60)	1.10990E+14	4.47179E+13	4.46033E+12

Table 3.1: Reference SERPENT values for single assembly calculations.

3.1.1 Full Radial Homogenization

The difference in axial power distribution (APD) as a function of temperature for the full radial homogenization test case is shown in Figure 3.2. Results show that this homogenization calculates the APD within 0.4% at 293 K and 0.6% at 800 K when compared to the reference solution.

Table 3.2 shows that, for this model, the diffusion solver significantly over-predicts the eigenvalue when compared to the reference SERPENT data.

When increasing from 293 K to 800 K, the overall contribution of the capture and leakage reaction rates for this model were found to increase by 5.51% and 15.22%, respectively (Table 3.3). These increases along with a 4.34% decrease in fission rate confirms spectral hardening in higher temperature calculations. Table 3.3 also shows that the total absorption reactions (i.e. captures and fissions) account for the vast majority of the calculated reactions in the TREAT

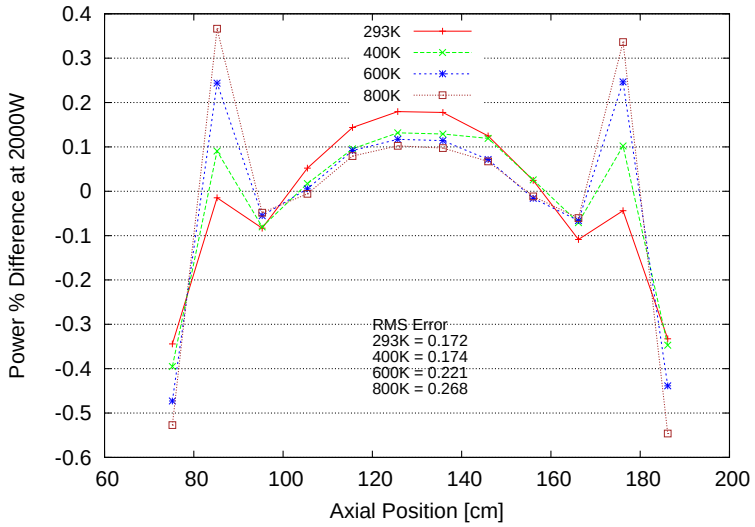

Figure 3.2: Full homogenization APD at 293 K, 400 K, 600 K, and 800 K.

Temp [K]	k_{eff} (pcm)	Diff Fiss Rate (%)	Diff Capt Rate (%)	Diff Leakage Rate (%)
293	1.43342 (582.84)	-0.829	-0.529	-17.966
400	1.41837 (631.98)	-0.885	-0.590	-18.262
600	1.39242 (695.10)	-0.968	-0.688	-17.951
800	1.37123 (756.71)	-1.027	-0.750	-18.065

Table 3.2: Diffusion results for the fully homogenized model.

system. It can therefore be inferred that these are the driving forces in the results shown in Table 3.2.

Spatial convergence of the mesh was ensured by uniformly refining the mesh by a factor of two. The calculated eigenvalue changed by 2.56 pcm with the absorption, fission, and capture changing by -0.10%, 0.00%, and -0.25%, respectively.

Because this specific homogenization does not have explicitly modeled air channels, it was solved with the P_N SAAF transport formulation. The purpose of this study was to observe transport effects through different anisotropy assumptions. Each of the data series in Figure 3.3 can be derived starting from the traditional, steady-state, multigroup P_1 equations (Equations

Temp [K]	Fission Rate Contrib. (%)	Capture Rate Contrib. (%)	Leakage Rate Contrib. (%)
293	58.99	38.29	2.89
400	58.37	38.81	2.99
600	57.30	39.68	3.17
800	56.43	40.40	3.33

Table 3.3: Percent contribution of individual reaction rates for full radial homogenization case.

3.2 and 3.3).

$$\nabla \cdot \mathbf{J_g} + \Sigma_{t_g}\phi_g = \sum_{g'=1}^{G} \Sigma_{s_{0,g'\to g}}\phi_{g'} + Q_g \tag{3.2}$$

$$\nabla \cdot \left(\frac{\phi_g}{3}\right) + \Sigma_{t_g}\mathbf{J_g} = \sum_{g'=1}^{G} \Sigma_{s_{1,g'\to g}}\mathbf{J_{g'}} \tag{3.3}$$

In the "P_1-isotropic" and "P_0" data series, the $\sum_{g'=1}^{G} \Sigma_{s_{1,g'\to g}}\mathbf{J_{g'}}$ term in Equation 3.3 is assumed to be zero (i.e. isotropy). Therefore, Equation 3.3 takes on the form:

$$\mathbf{J_g} = -\frac{1}{3\Sigma_{t_g}}\nabla\phi_g = -D\nabla\phi_g \tag{3.4}$$

Plugging Equation 3.4 (Fick's Law) into Equation 3.2, one can obtain the traditional, steady-state diffusion equation:

$$-\nabla \cdot D\nabla\phi_g + \Sigma_{t_g}\phi_g = \sum_{g'=1}^{G} \Sigma_{s_{0,g'\to g}}\phi_{g'} + Q_g \tag{3.5}$$

The difference between the results for the "P_1-isotropic" and "P_0" data series in Figure 3.3 is due to the odd-even parity coupling by the boundary condition.

In the "Diffusion" data series of Figure 3.3, Equation 3.5 is used with the exception that the diffusion coefficient, "D", is represented with a transport corrected total cross section.

$$\mathbf{J_g} = -\frac{1}{3\left(\Sigma_{t_g} - \sum_{g'=1}^{G} \Sigma_{s_{1,g\to g}}\right)}\nabla\phi_g = -\frac{1}{3\Sigma_{tr_g}}\nabla\phi_g = -D\nabla\phi_g \tag{3.6}$$

For the "P_1-anisotropic" and "P_3" data series, the fully coupled set of P_1 equations (Equations 3.2 and 3.3) are utilized. Figure 3.3 shows that by increasing the moments of the group-to-group and within-group scattering matrices, no improvements are obtained.

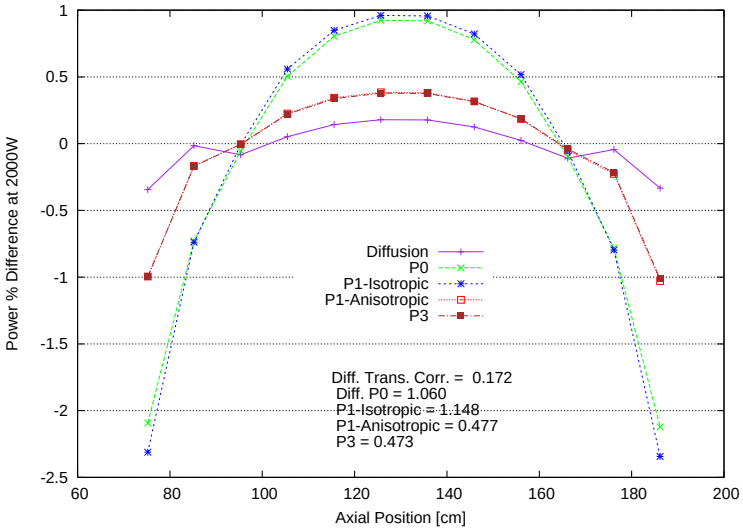

Figure 3.3: Full homogeneous APD for Pn transport solutions.

Table 3.4 shows the transport calculated eigenvalues and reaction rates within MAMMOTH at 293 K.

P_n Order	k_{eff} (pcm)	Diff Fiss Rate (%)	Diff Capt Rate (%)	Diff Leakage Rate (%)
Diff	1.43342 (582.84)	-0.829	-0.529	-17.966
P_0	1.44703 (1235.82)	-1.762	-2.065	-27.774
P_1-Iso	1.44723 (1245.42)	-1.775	-2.199	-26.700
P_1-Aniso	1.43693 (750.05)	-1.071	-1.118	-18.347
P_3	1.43622 (718.847)	-1.022	-1.114	-17.120

Table 3.4: Transport results for the fully homogenized model.

3.1.2 Full Main Homogenization with Explicit Cooling Channels & Interassembly Gaps

In order to properly model the explicit cooling channels and interassembly gaps, a sensitivity study of the diffusion coefficient treatment was completed. In this study, the group wise diffusion coefficients generated from DRAGON were artificially adjusted via multiplicative constants to minimize the relative error in the APD computed by MAMMOTH. Figure 3.4 shows the results from this study.

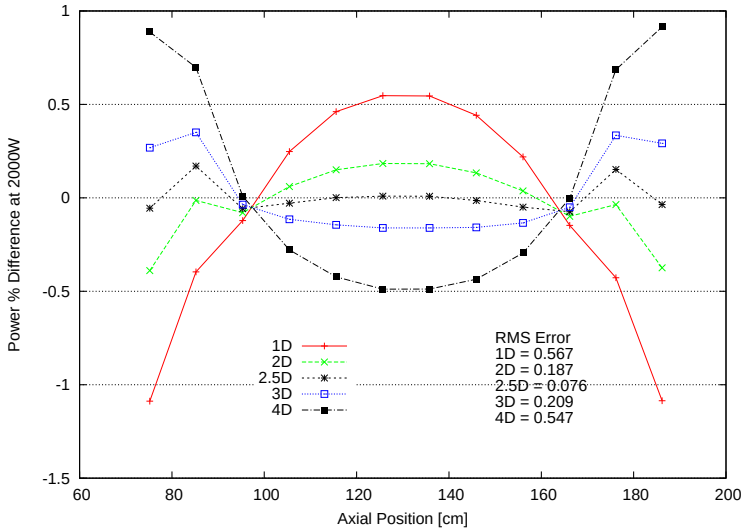

Figure 3.4: Diffusion constant study for full fuel with explicit channels assembly model. Data series notation is as follows: ($Mult.Const.$) x D

Behaviors observed in this study are strictly based on the calculation of the neutron population within the fuel. 1D (nominal case from DRAGON) results over-predict the neutron population in the center of the fuel and under-predict the neutron population near the fuel/reflector interface. As the diffusion coefficient is increased, more neutrons are forced out of the fuel and into the reflectors where they are thermalized. This adjustment affects the incoming partial current into the fuel region and increases the fission rate in the fuel near the periphery. This behavior can especially be seen for the highly diffuse, 4D test case. The case that produces the best neutron balance is when the diffusion coefficient is increased by a factor of 2.5. This results in an RMS deviation of 0.076% compared to reference SERPENT calculations, and was chosen as the effective diffusion coefficient for this homogenization model.

Figure 3.5 shows the difference in calculated power distribution from the reference solution as

a function of temperature for this homogenization. By explicitly modeling the cooling channels and interassembly gaps, there are significant improvements over the fully homogeneous model. Similar behavior can be observed at the periphery of the fuel as in the fully homogeneous model of Section 3.1.1.

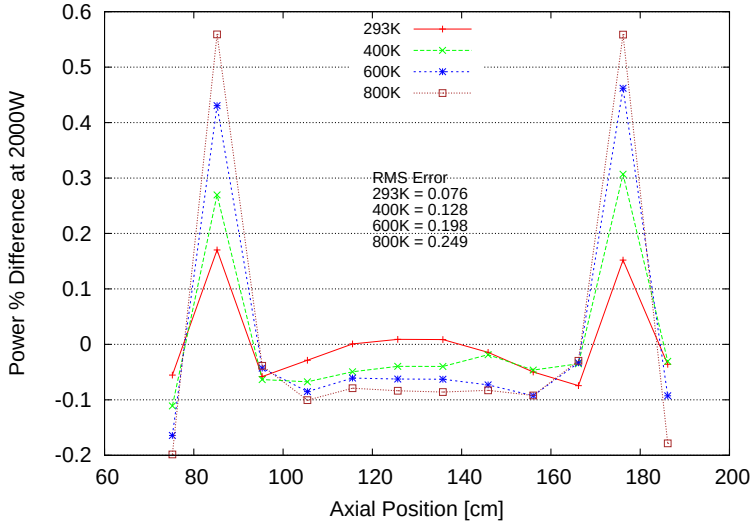

Figure 3.5: APD for full main homogenization with explicit channel modeling.

Table 3.5 shows the integral reaction rates for this homogenization approach. Some improvements are observed compared to the results in Table 3.2. Because of the marginal improvement in integral reaction rates and simultaneous significant improvement in power distribution, we presume that the reaction rate error is driven by unresolved differences within the reflector region.

Temp [K]	k_{eff} (pcm)	Diff Fiss Rate (%)	Diff Capt Rate (%)	Diff Leakage Rate (%)
293	1.43190 (508.85)	-0.723	-0.586	-16.605
400	1.41682 (554.59)	-0.776	-0.643	-16.930
600	1.39088 (614.58)	-0.852	-0.741	-16.700
800	1.36963 (671.44)	-0.912	-0.800	-16.807

Table 3.5: Diffusion results for the full main with explicit channels model.

Table 3.6 shows the contribution percentage for the reaction rates as a function of temperature. When comparing these results to that of Table 3.3 it is clear that by explicitly modeling the channels and interassembly gaps has little effect on the reaction rate contribution percentages.

Temp [K]	Fission Rate Contrib. (%)	Capture Rate Contrib. (%)	Leakage Rate Contrib. (%)
293	58.93	38.29	2.93
400	58.31	38.75	3.03
600	57.24	39.62	3.22
800	56.36	40.34	3.37

Table 3.6: Percent contribution of individual reaction rates for full main homogenization case.

Spatial convergence of the mesh was ensured by uniformly refining the mesh by a factor of two. The calculated eigenvalue changed by 5.33 pcm with the absorption, fission, and capture changing by -0.10%, 0.00%, and -0.26%, respectively.

3.1.3 Clad Gap, Clad, Cooling Channel, & Interassembly Gap Homogenization

High order P_N transport calculations were allowed to be completed due to the fact that this model homogenizes the air channels and interassembly gaps with the clad. Figures 3.6 and 3.7 show the difference in APD from the SERPENT reference solution as a function of temperature and angular refinement. Poor diffusion results are expected for this model because in homogenizing the air channels and interassembly gaps, accuracy of the known diffusive characteristics of these channels is lost.

Data shown in Figures 3.6 and 3.7 show a strong angular dependence in the streaming of the assemblies. This dependence is discussed in greater detail in Section 4.3.

Tables 3.7 and 3.8 show the reaction rates for this homogenization at 293 K and 800 K, respectively. As expected, as the angular discretization order is increased, calculated reaction rates compare more closely with the reference results. Angular convergence is shown with 17th order refinement.

Table 3.9 shows the difference in reaction rates from the reference solution as a function of temperature. Compared to the results to that of Table 3.3, increasing the fidelity of the angular

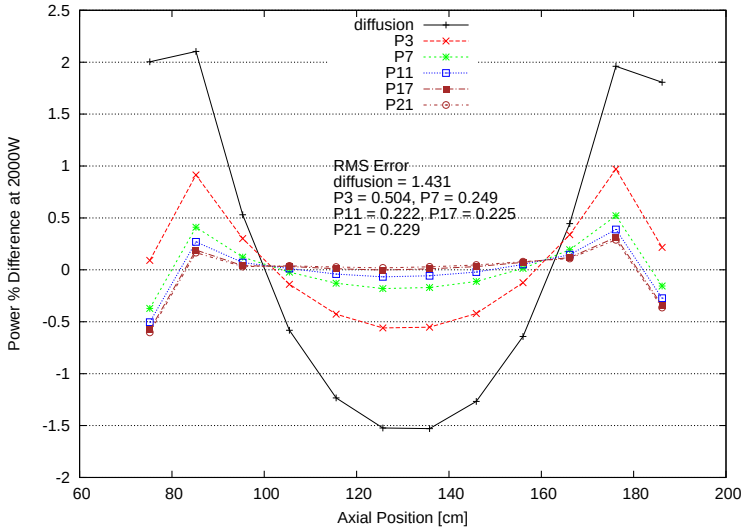

Figure 3.6: APD comparison for diffusion and Pn transport solves at 293 K. The lower reported RMS for the 11th order solution is due to a cancellation of error between the center and periphery of the fuel.

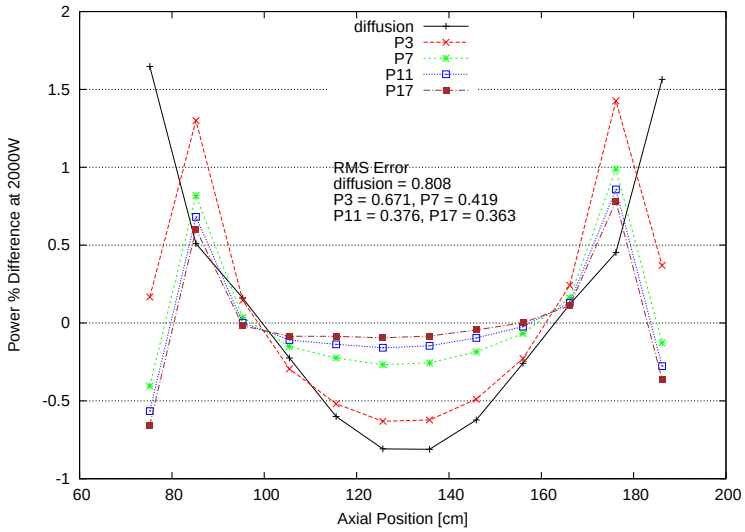

Figure 3.7: APD comparison for diffusion and Pn transport solves at 800 K.

discretization has little effect on the reaction rate contribution percentages.

Spatial convergence of the mesh was ensured by uniformly refining the mesh by a factor of two. The calculated eigenvalue changed by 30.0 pcm with the absorption, fission, and capture changing by -0.19%, 0.00%, and -0.45%, respectively.

Pn Order	k_{eff} (pcm)	Diff Fiss Rate (%)	Diff Capt Rate (%)	Diff Leakage Rate (%)
3	1.40080 (-1041.03)	1.480	1.671	24.115
7	1.41838 (-156.76)	0.223	0.360	2.439
11	1.42328 (85.84)	-0.122	-0.014	-3.354
17	1.42609 (221.22)	-0.319	-0.220	-6.625
21	1.42700 (268.44)	-0.382	-0.299	-7.677

Table 3.7: Pn transport results for various angular orders at 293 K.

Pn Order	k_{eff} (pcm)	Diff Fiss Rate (%)	Diff Capt Rate (%)	Diff Leakage Rate (%)
3	1.33226 (-1374.32)	1.864	2.113	25.208
7	1.35306 (-220.30)	0.2980	0.469	2.722
11	1.35889 (96.31)	-0.132	-0.001	-3.278
17	1.36224 (277.62)	-0.378	-0.270	-6.688

Table 3.8: Pn transport results for various angular orders at 800 K.

Temp [K]	Fission Rate Contrib. (%)	Capture Rate Contrib. (%)	Leakage Rate Contrib. (%)
293	58.69	38.21	3.27
400	58.04	38.73	3.40
600	56.96	39.62	3.58
800	56.06	40.33	3.76

Table 3.9: Percent contribution of individual reaction rates for P17 quadrature order for clad, clad gap, channel, and interassembly gap homogenization case.

3.1.4 Clad Gap and Clad Homogenization

In this model, the clad gap and clad are homogenized together leaving the interassembly gaps and cooling channels explicitly modeled. As before in Section 3.1.2 a diffusion coefficient study

was completed to obtain an optimized diffusion coefficient (Figure 3.8). The results from this study showed that the nominal diffusion coefficient, 1D, produced the most accurate results when compared to the reference SERPENT solution.

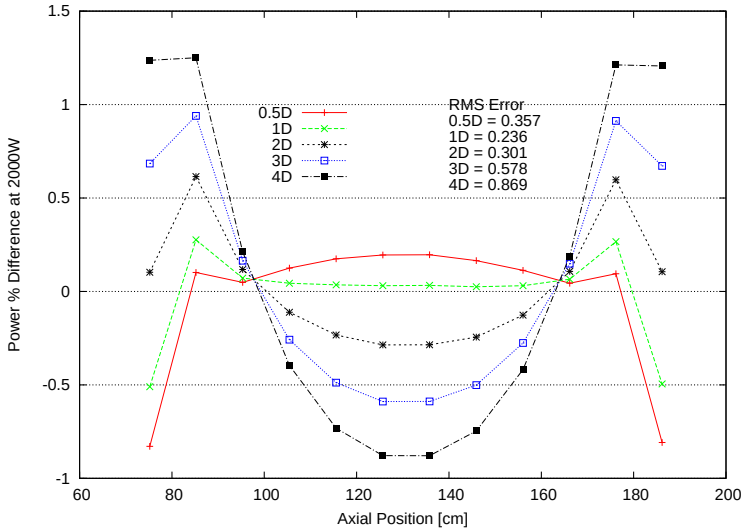

Figure 3.8: Clad gap and clad homogenization diffusion constant study.

Figure 3.9 shows the difference in the APD from the reference SERPENT results for the clad gap and clad homogenization scheme. Figure 3.5 shows a lower RMS difference than that of Figure 3.9. However, the center of the fueled regions produce results of similar accuracy. For Figure 3.5 and Figure 3.9 the center cross section region produces RMS deviations from the reference solution of 0.026% and 0.043%, respectively. These differences are suspected to be approaching the convergence limit of the model (i.e. number of spatial cross section regions - see Section **??**). Further improvements were not investigated due to the models being within the physically measurable limits of the TREAT system.

Table 3.10 shows comparisons of calculated eigenvalues and associated reaction rates with reference results for this model. Compared with Table 3.5, significant improvements are made in the leakage rates, slight improvements are made in the fission source, and the capture reaction rates are less accurately calculated.

Table 3.11 shows the contribution percentage for the reaction rates as a function of temperature.

Spatial convergence of the mesh was ensured by uniformly refining the mesh by a factor of two. The calculated eigenvalue changed by 11.25 pcm with the absorption, fission, and capture

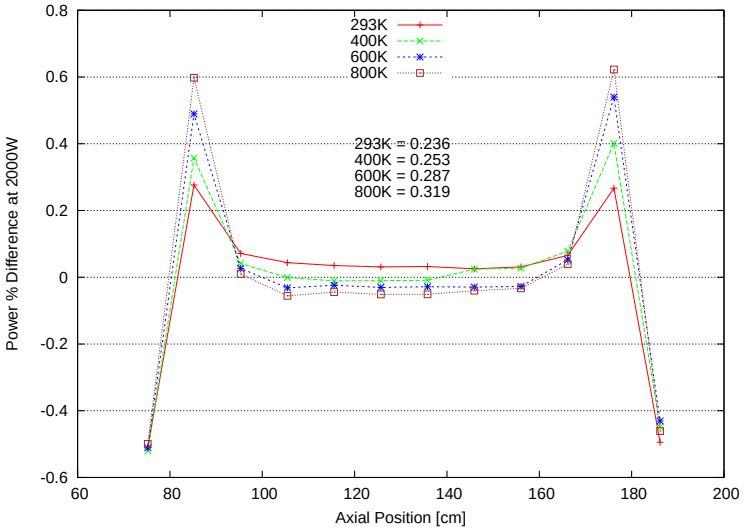

Figure 3.9: Clad gap and clad homogenization APD.

Temp [K]	k_{eff} (pcm)	Diff Fiss Rate (%)	Diff Capt Rate (%)	Diff Leakage Rate (%)
293	1.41173 (-488.81)	0.695	0.839	8.451
400	1.39565 (-515.67)	0.729	0.890	8.259
600	1.36816 (-579.38)	0.794	0.947	8.861
800	1.34580 (-621.37)	0.843	1.001	8.791

Table 3.10: Diffusion results for the clad gap and clad homogenization model.

Temp [K]	Fission Rate Contrib. (%)	Capture Rate Contrib. (%)	Leakage Rate Contrib. (%)
293	58.10	38.23	3.76
400	57.43	38.76	3.89
600	56.30	39.63	4.14
800	55.38	40.35	4.34

Table 3.11: Percent contribution of individual reaction rates for clad and clad gap homogenization case.

changing by -0.08%, 0.00%, and -0.20%, respectively.

3.1.5 Full Heterogeneous

In this model, all radial volumes are explicitly modeled. A diffusion study like that of Sections 3.1.2 and 3.1.4 was completed. In this study it was found that the 2D test case produced the most accurate results when compared to the reference SERPENT solutions.

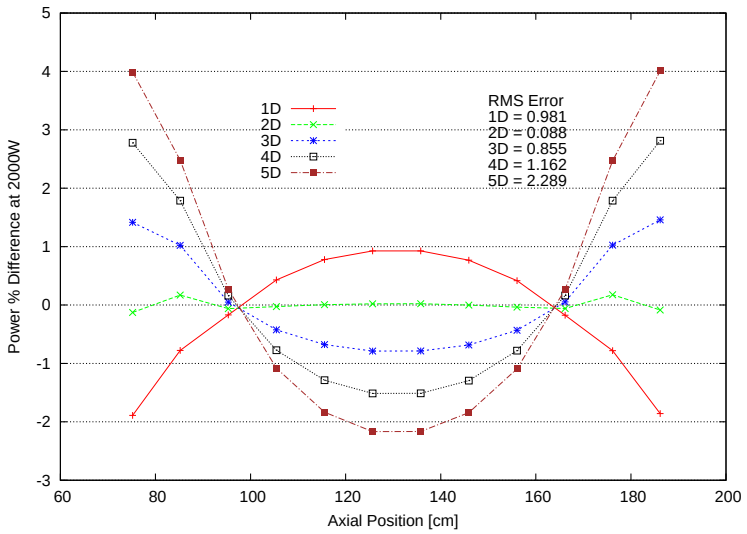

Figure 3.10: Heterogeneous homogenization diffusion constant study.

Figure 3.11 shows the difference in APD from the reference calculation for this model. Like that of the more complex homogenization models, the deviations are reduced in the center of fuel, increasing near the peripheries.

Table 3.12 shows the reaction rates and eigenvalue calculated for this model. This model gives the most accurate eigenvalue compared with reference SERPENT solutions. However, there are still cancellation of errors between the under-predicted leakage and over-predicted capture reaction rates. The same pattern emerges with accurate predictions for the central fuel region and less accuracy near the peripheries.

Table 3.13 shows the contribution percentage for the reaction rates as a function of temperature.

Spatial convergence of the mesh was ensured by uniformly refining the mesh by a factor of two. The calculated eigenvalue changed by 6.05 pcm with the absorption, fission, and capture

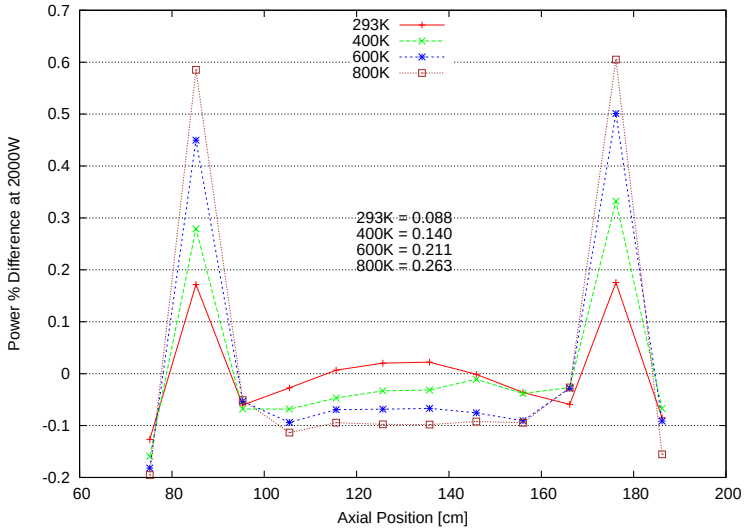

Figure 3.11: Heterogeneous homogenization APD.

Temp [K]	k_{eff} (pcm)	Diff Fiss Rate (%)	Diff Capt Rate (%)	Diff Leakage Rate (%)
293	1.41676 (-237.27)	0.337	1.421	-10.519
400	1.40095 (-244.91)	0.348	1.504	-11.132
600	1.37362 (-288.51)	0.393	1.563	-10.191
800	1.35206 (-277.48)	0.376	1.559	-10.571

Table 3.12: Diffusion results for the heterogeneous model.

Temp [K]	Fission Rate Contrib. (%)	Capture Rate Contrib. (%)	Leakage Rate Contrib. (%)
293	58.30	38.59	3.11
400	57.65	38.14	3.21
600	56.53	40.03	3.43
800	55.64	40.77	3.58

Table 3.13: Percent contribution of individual reaction rates for heterogeneous model.

changing by -0.10%, 0.00%, and -0.25%, respectively.

3.1.6 Model Comparison

Figure 3.12 shows the calculated APD for each of the modeling approaches. As shown in the detailed analysis of Sections 3.1.1 through 3.1.5, the models with greater heterogeneity perform best in the central fuel region with varying degrees of error in the peripheries.

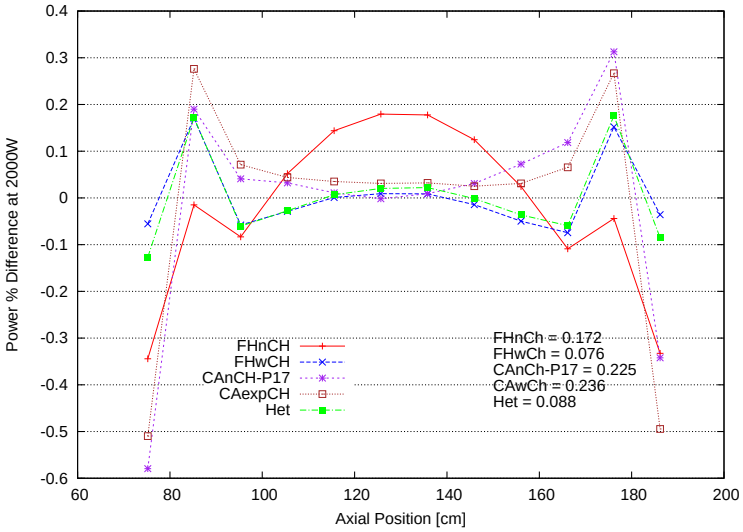

Figure 3.12: APD model comparison at 293 K.

3.2 Minimum Critical Core Calculations

Reference reaction rates for the minimum critical core are shown in Table 3.14. The reference axially integrated radial power distribution (RPD) and radially integrated axial power distribution (APD) at 293 K are shown in Figures 3.13 and 3.14. The effect of the control assemblies present at the top of the core within the reflector region is evident in the power depression at the top of Figure 3.14. Because of the control assembly location, the axial offset of this core configuration is -3.26% (Equation 3.7).

$$\text{Offset } \% = \frac{\sum_{level=7}^{12} Power - \sum_{level=1}^{6} Power}{\sum_{level=1}^{12} Power} * 100 \tag{3.7}$$

Temp [K]	k_{eff} (pcm)	Fission Source Rate	Capture Rate	Leakage Rate
293	1.00540 (1.7)	1.49842E+14	7.46122E+13	1.34098E+13
400	0.98034 (1.7)	1.53676E+14	7.77201E+13	1.41323E+13
600	0.94052 (1.8)	1.60191E+14	8.29971E+13	1.53667E+13
800	0.90882 (1.8)	1.65783E+14	8.75126E+13	1.64387E+13

Table 3.14: Reference SERPENT values for minimum critical core configuration. Uncertainty reported for eigenvalues are statistical uncertainty.

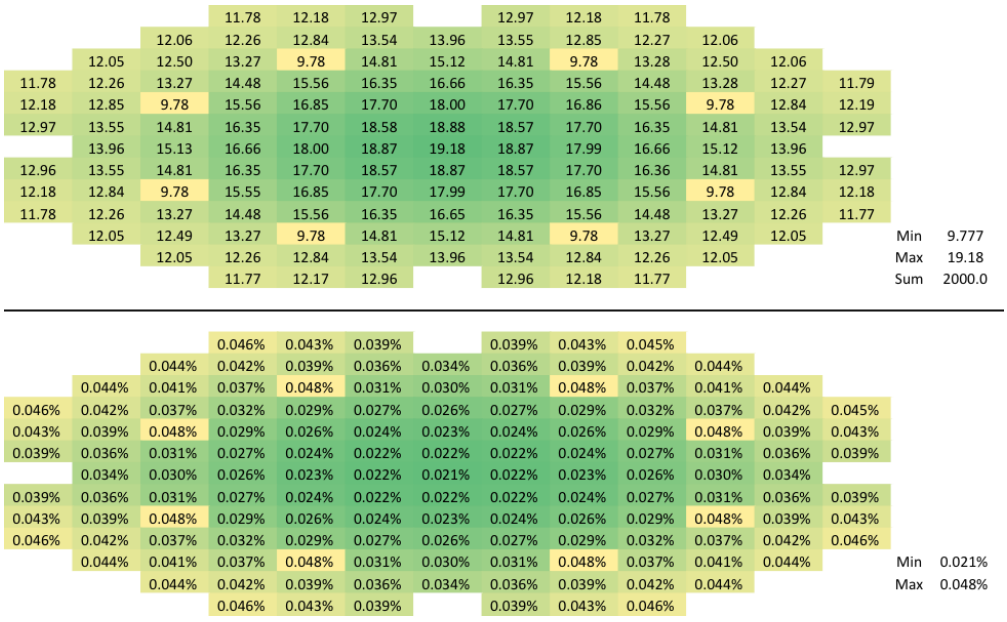

Figure 3.13: Reference solution for the axially-integrated, radial power distribution. Top figure is the raw distribution while the bottom is the statistical uncertainty associated with the simulation.

Sections 3.2.1 and 3.2.2, and 3.2.3 discuss calculated results for the various modeling approaches. In each of the models analyzed, the near void regions are ascribed modified diffusion coefficients based on the relevant standard assembly calculations. This representation does not account for spectral effects from the control assemblies and therefore the reflector and core re-

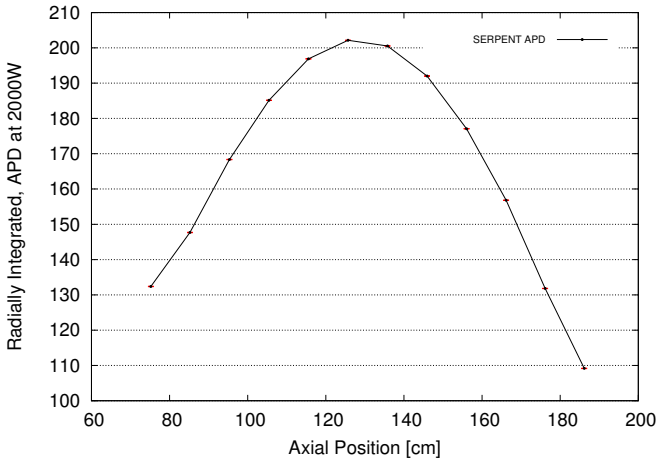

Figure 3.14: Reference solution for the radially integrated, axial power distribution. APD error bars are shown in red.

action rates will be affected. More detailed control assembly modeling is left for future work and is discussed in Section 4.4.

3.2.1 Full Radial Homogenization

The air gap between the main core and the CP-2 graphite was given a diffusion coefficient of 2.5D.

Figure 3.15 shows the difference from the reference RPD for this model. When compared to the reference SERPENT solution, the RMS deviation is 0.316% with a maximum and minimum deviation of 0.440% and -0.630%, respectively. The spatial deviation in the RPD is smallest between the center and periphery of the core. This distribution can be explained by the cross section preparation process. Cross sections for the different assembly types are weighted over the average flux of the entire core - see Figure 2.14. This averaged flux is numerically closest to the reference flux somewhere between the center and periphery of the core, causing the smallest deviation in power to be between the center and periphery of the core.

Figure 3.16 shows the deviation from the reference APD for this homogenization of the minimum critical core. Results are similar to those from the single assembly calculations. The smallest difference from the reference calculation for each temperature case occurs in the center of the core with the increasing deviation at the peripheries due to the increased flux gradient.

Table 3.15 shows the calculated reaction rates for the fully homogenized model. This ho-

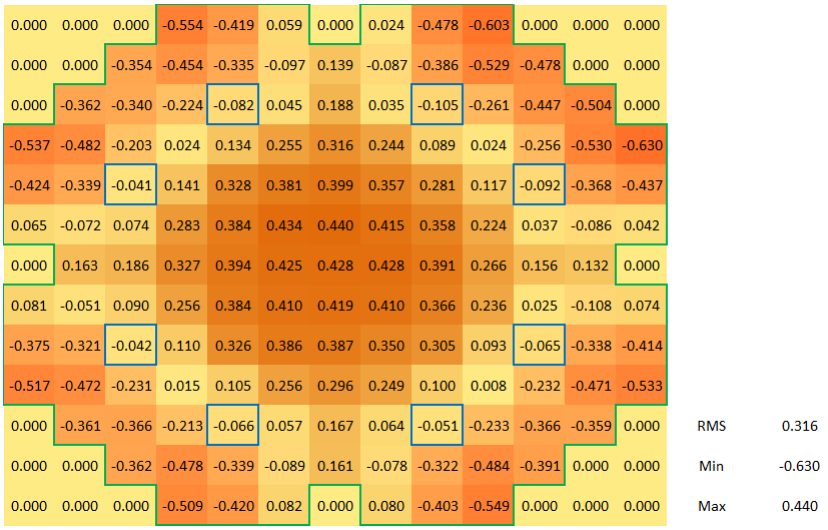

Figure 3.15: RPD for fully homogenized minimum critical core configuration. The active core is outlined in green and control assemblies are outlined in blue.

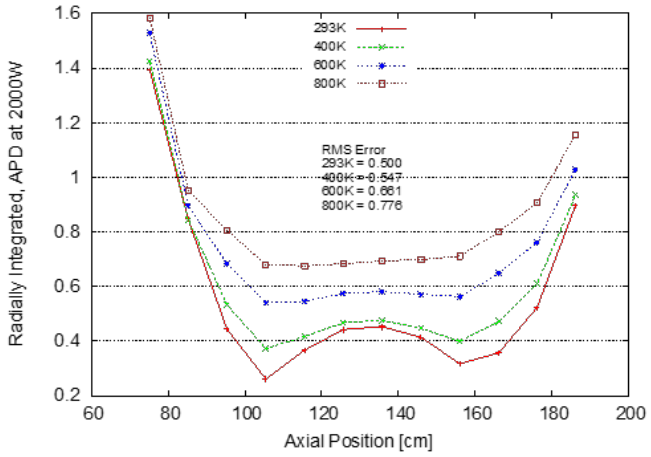

Figure 3.16: APD for the fully homogenized minimum critical core configuration.

mogenization significantly over-predicts the eigenvalue from reference SERPENT solutions. The reason for this large over-prediction is due to the large under-prediction of integral captures. Because the power distribution is relatively accurate, it can be inferred that the capture reactions are being mispredicted in the axial and radial reflector regions.

Table 3.16 shows the contribution percentage for the reaction rates as a function of temperature. When increasing from 293 K to 800 K, the overall contribution of the capture and leakage reaction rates for this model were found to increase 5.73% and 9.06%, respectively. These in-

Temp [K]	k_{eff} (pcm)	Diff Fiss Rate (%)	Diff Capt Rate (%)	Diff Leakage Rate (%)
293	1.01961 (1388.79)	-1.407	-13.518	33.963
400	0.99509 (1509.00)	-1.498	-13.339	31.440
600	0.95590 (1710.37)	-1.630	-13.723	31.392
800	0.92462 (1879.18)	-1.732	-14.034	31.429

Table 3.15: Diffusion results for the fully homogenized model.

creases along with a 9.32% decrease in fission rate confirms spectral hardening in temperature dependent calculations. The values for each temperature in Table 3.16 do not sum to 100% because captures in the permanent reflector region were not included.

Temp [K]	Fission Rate Contrib. (%)	Capture Rate Contrib. (%)	Leakage Rate Contrib. (%)
293	41.96	43.68	12.16
400	40.95	44.49	12.27
600	39.38	45.44	12.81
800	38.05	46.18	13.26

Table 3.16: Percent contribution of individual reaction rates for full homogenization case.

Spatial convergence of the mesh was ensured by uniformly refining the mesh by a factor of two. The calculated eigenvalue changed by 21.02 pcm with the absorption, fission, and capture changing by -0.01%, -0.01%, and -0.04%, respectively.

3.2.2 Full Main Homogenization with Explicit Cooling Channels and Interassembly Gaps

In this model, all of the cooling channels, interassembly gaps, and the gap between the CP-2 permanent reflector and core are treated with a diffusion coefficient of 2.5D.

Figure 3.17 shows the difference from the reference RPD for this homogenization. As observed in the standard assembly results, by explicitly modeling the channels and gaps, the

agreement with the reference power distribution is improved by 29.7% over that of the full radial homogenization. As before in Figure 3.15, the deviation in the RPD for this test case has the same shape with the highest relative error in the center and at the peripheries of the core.

0.000	0.000	0.000	-0.464	-0.354	0.007	0.000	-0.020	-0.381	-0.514	0.000	0.000	0.000
0.000	0.000	-0.277	-0.309	-0.238	-0.012	0.144	-0.019	-0.253	-0.362	-0.346	0.000	0.000
0.000	-0.266	-0.194	-0.144	-0.032	0.045	0.153	0.057	-0.059	-0.160	-0.241	-0.352	0.000
-0.470	-0.303	-0.144	0.013	0.074	0.184	0.209	0.177	0.055	0.019	-0.162	-0.337	-0.537
-0.351	-0.264	-0.041	0.074	0.196	0.249	0.240	0.224	0.186	0.072	-0.035	-0.242	-0.396
-0.022	-0.042	0.053	0.168	0.223	0.251	0.261	0.281	0.256	0.173	0.069	-0.011	0.007
0.000	0.127	0.140	0.211	0.235	0.277	0.279	0.274	0.265	0.208	0.162	0.158	0.000
0.042	-0.019	0.062	0.175	0.242	0.269	0.281	0.270	0.242	0.158	0.048	-0.033	-0.006
-0.327	-0.191	-0.030	0.112	0.194	0.245	0.261	0.238	0.201	0.072	-0.041	-0.215	-0.344
-0.461	-0.277	-0.112	0.026	0.077	0.182	0.235	0.183	0.069	0.034	-0.090	-0.268	-0.432
0.000	-0.252	-0.168	-0.137	-0.054	0.057	0.161	0.080	-0.019	-0.104	-0.164	-0.232	0.000
0.000	0.000	-0.212	-0.301	-0.213	0.012	0.180	-0.005	-0.181	-0.245	-0.237	0.000	0.000
0.000	0.000	0.000	-0.421	-0.302	0.024	0.000	0.032	-0.317	-0.411	0.000	0.000	0.000

RMS	0.22276626
MAX	0.28121458
MIN	-0.5368345

Figure 3.17: RPD for the full main homogenization with explicit channels for the minimum critical core configuration. The active core is outlined in green and control assemblies are outlined in blue.

The deviation from the reference APD for this model (Figure 3.18) shows higher RMS values than that of the previous model (Figure 3.16). As seen before in the standard assembly calculations of Section 3.1, the error distribution in the center region of the fuel improves to 0.055%. The increased error on the top of the core reported in Figure 3.18 is caused by the modeling of the control assemblies and is the driving factor in the increase in total RMS deviation.

Table 3.17 shows the associated reaction rates and eigenvalues for this model. Calculated eigenvalued are significantly improved when compared to that of the results of Table 3.15. The reason for this improvement however is simply due to a cancellation of error with the capture and leakage rates. The fission rate, however, has improved dramatically.

Table 3.18 shows the contribution percentage for the reaction rates as a function of temperature. As observed in the single assembly calculations of Section 3.1.2, explicit modeling of the cooling channels and interassembly gaps did not affect the reaction rate contribution percentages.

Spatial convergence of the mesh was ensured by uniformly refining the mesh by a factor of two. The calculated eigenvalue changed by -69.19 pcm with the absorption, fission, and capture

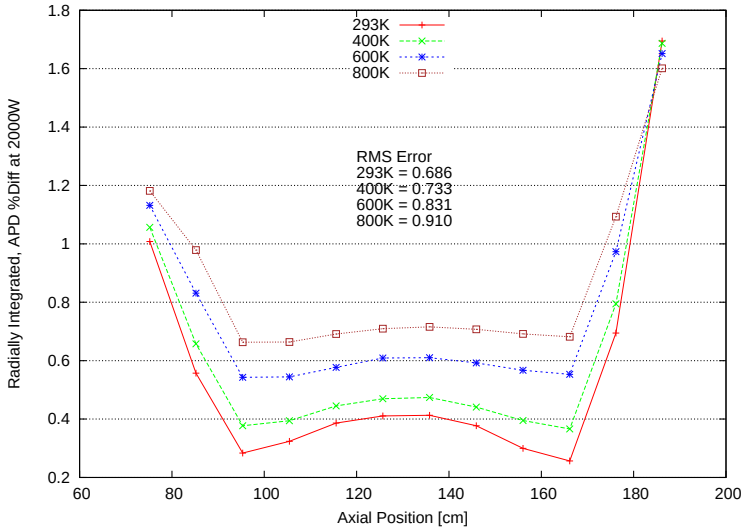

Figure 3.18: APD for the full main homogenization with explicit channels for the minimum critical core configuration.

Temp [K]	k_{eff} (pcm)	Diff Fiss Rate (%)	Diff Capt Rate (%)	Diff Leakage Rate (%)
293	1.00575 (24.68)	-0.056	-12.180	40.195
400	0.98104 (73.21)	-0.095	-12.402	40.149
600	0.94159 (131.24)	-0.128	-12.746	40.181
800	0.91019 (166.12)	-0.172	-12.996	40.168

Table 3.17: Diffusion results for the full main homogenization with explicit channels model.

Temp [K]	Fission Rate Contrib. (%)	Capture Rate Contrib. (%)	Leakage Rate Contrib. (%)
293	41.39	43.68	12.16
400	40.37	44.49	12.27
600	38.75	45.44	12.81
800	37.46	46.18	13.26

Table 3.18: Percent contribution of individual reaction rates for full radial homogenization case.

changing by -0.22%, 0.00%, and -0.43%, respectively.

3.2.3 Full Heterogeneous

In this model the clad gap, channels, interassembly gaps, and air gap between the core and CP-2 graphite were treated with a diffusion coefficient adjusted by a factor of 2D.

Figure 3.19 shows the difference from the reference RPD for this model. The reported RMS deviation increased by a factor of 4.69 to 1.041% when compared to the fully homogenized with explicit channels model of Section 3.2.2. The reason for this increase is due to improper diffusion coefficient treatment of the clad gap region.

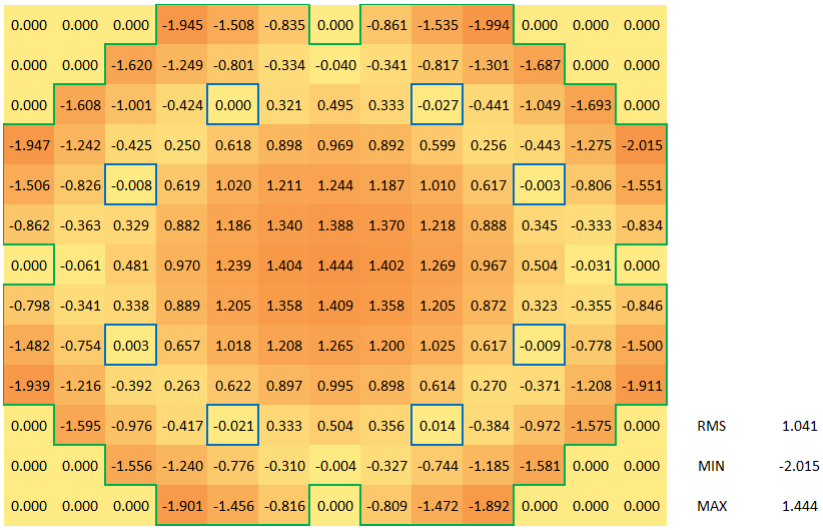

Figure 3.19: RPD for heterogeneous minimum critical core configuration. The active core is outlined in green and control assemblies are outlined in blue.

Figure 3.20 shows the deviation from the reference APD for this model. A similar distribution of error that is driven by flux gradients and improper control rod modeling is shown.

Table 3.19 shows the reaction rates and calculated eigenvalues for this core configuration. The observed over-prediction of the leakage and under-prediction of capture reactions suggests that the material properties of the core are too diffuse and too many neutrons are being forced out of the system. Near void regions (i.e. clad gap, interassembly gaps, and channels) are being treated with a diffusion coefficient that is too high and does not accurately calculate the physics of the core.

Table 3.20 shows the contribution percentage for the reaction rates as a function of temper-

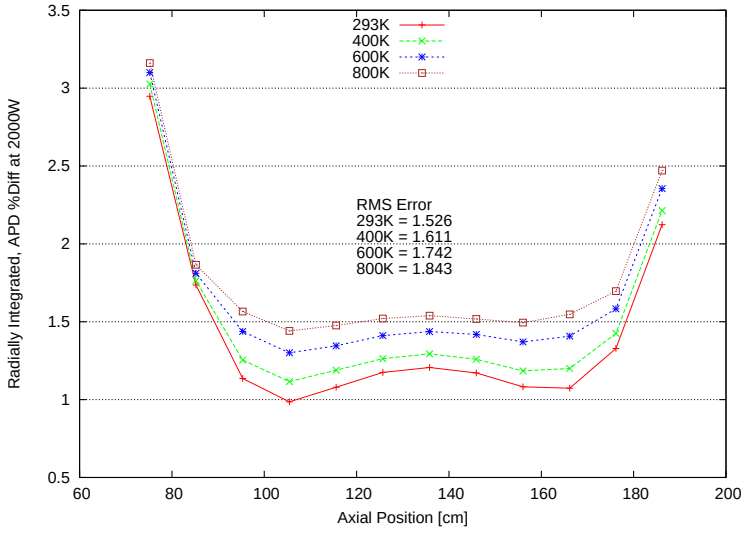

Figure 3.20: APD for the heterogeneous minimum critical core configuration.

Temp [K]	k_{eff} (pcm)	Diff Fiss Rate (%)	Diff Capt Rate (%)	Diff Leakage Rate (%)
293	1.02073 (1493.80)	-1.523	-9.500	32.966
400	0.99623 (1626.51)	-1.617	-9.659	32.905
600	0.95717 (1860.91)	-1.754	-9.969	32.777
800	0.92599 (2040.71)	-1.875	-10.194	32.759

Table 3.19: Diffusion results for the heterogeneous model.

ature.

Temp [K]	Fission Rate Contrib. (%)	Capture Rate Contrib. (%)	Leakage Rate Contrib. (%)
293	42.01	45.78	12.08
400	41.00	46.44	12.42
600	39.39	47.49	12.96
800	38.11	48.31	13.42

Table 3.20: Percent contribution of individual reaction rates for heterogeneous case.

Spatial convergence of the mesh was ensured by uniformly refining the mesh by a factor of two. The calculated eigenvalue changed by -13.22 pcm with the absorption, fission, and capture changing by -0.02%, 0.00%, and -0.04%, respectively.

3.3 Preliminary Improvements on Minimum Critical Core Calculations

Preliminary calculations have been completed showing improvements in power distributions for the minimum critical core configuration. A common issue seen in all of the homogenization models was the spatial distribution of the deviation from the reference RPD. Figures 3.15, 3.17, and 3.19 showed the highest errors in the center of the core and at the peripheries. Realistically, the largest deviations should be at the peripheries with the smallest deviations being at the center of the core. In order to see this expected distribution, the fuel assemblies were split into three separate cross section regions (Figure 3.21).

	A	B	C	D	E	F	G	H	J	K	L	M	N	O	P	R	S	T	U
1	6	6	6	6	6	6	6	6	6	6	6	6	6	6	6	6	6	6	6
2	6	6	6	6	6	6	6	6	6	6	6	6	6	6	6	6	6	6	6
3	6	6	6	6	6	6	5	5	5	6	5	5	5	6	6	6	6	6	6
4	6	6	6	6	6	5	3	3	3	5	3	3	3	5	6	6	6	6	6
5	6	6	6	6	5	3	2	2	2	3	2	2	2	3	5	6	6	6	6
6	6	6	6	5	3	1	2	4	2	1	2	4	2	1	3	5	6	6	6
7	6	6	5	3	2	2	2	2	2	1	2	2	2	2	2	3	5	6	6
8	6	6	5	3	2	4	2	1	1	1	1	1	2	4	2	3	5	6	6
9	6	6	5	3	2	2	2	1	1	1	1	1	2	2	2	3	5	6	6
10	6	6	6	5	1	1	1	1	1	1	1	1	1	1	1	5	6	6	6
11	6	6	5	3	2	2	2	1	1	1	1	1	2	2	2	3	5	6	6
12	6	6	5	3	2	4	2	1	1	1	1	1	2	4	2	3	5	6	6
13	6	6	5	3	2	2	2	2	2	1	2	2	2	2	2	3	5	6	6
14	6	6	6	5	3	1	2	4	2	1	2	4	2	1	3	5	6	6	6
15	6	6	6	6	5	3	2	2	2	3	2	2	2	3	5	6	6	6	6
16	6	6	6	6	6	5	3	3	3	5	3	3	3	5	6	6	6	6	6
17	6	6	6	6	6	6	5	5	5	6	5	5	5	6	6	6	6	6	6
18	6	6	6	6	6	6	6	6	6	6	6	6	6	6	6	6	6	6	6
19	6	6	6	6	6	6	6	6	6	6	6	6	6	6	6	6	6	6	6

1	Fuel Assembly 1	4	Control Assembly
2	Fuel Assembly 2	5	Al Clad Dummy Assembly
3	Fuel Assembly 3	6	Zr Clad Dummy Assembly

Figure 3.21: Modified minimum critical core map including separate fuel cross section regions.

Figure 3.22 shows the deviation from the reference RPD for the modified, fully homogeneous minimum critical core. By adding these cross section regions, the error is more evenly distributed as expected, and in turn, the overall error statistics are reduced.

0.000	0.000	0.000	-0.120	0.049	0.501	0.000	0.474	0.022	-0.169	0.000	0.000	0.000	
0.000	0.000	-0.037	-0.479	-0.365	-0.046	0.544	-0.053	-0.380	-0.531	-0.104	0.000	0.000	
0.000	-0.021	-0.494	-0.351	-0.083	-0.052	-0.008	-0.039	-0.109	-0.367	-0.541	-0.106	0.000	
-0.111	-0.460	-0.344	-0.092	0.027	0.152	0.068	0.146	0.008	-0.085	-0.361	-0.493	-0.179	
0.072	-0.370	-0.074	0.037	0.091	0.164	0.157	0.140	0.081	0.035	-0.069	-0.350	0.027	
0.461	-0.163	-0.052	0.152	0.145	0.203	0.231	0.233	0.178	0.157	-0.036	-0.133	0.489	
0.000	-0.091	-0.100	0.086	0.161	0.249	0.270	0.247	0.191	0.083	-0.077	-0.060	0.000	
0.526	-0.140	-0.042	0.158	0.165	0.221	0.251	0.221	0.165	0.142	-0.057	-0.154	0.477	
0.097	-0.298	-0.062	0.076	0.090	0.162	0.179	0.154	0.096	0.036	-0.074	-0.322	0.080	
-0.101	-0.433	-0.310	-0.077	0.032	0.152	0.095	0.152	0.024	-0.070	-0.289	-0.425	-0.073	
0.000	-0.005	-0.466	-0.342	-0.102	-0.038	0.002	-0.015	-0.068	-0.310	-0.463	0.014	0.000	RMS 0.247
0.000	0.000	0.032	-0.467	-0.337	-0.020	0.583	-0.037	-0.305	-0.413	0.005	0.000	0.000	Min -0.541
0.000	0.000	0.000	-0.072	0.105	0.522	0.000	0.530	0.089	-0.063	0.000	0.000	0.000	Max 0.583

Figure 3.22: RPD for fully homogenized, modified minimum critical core configuration. The active core is outlined in green and control assemblies are outlined in blue.

Figure 3.23 shows the deviation from the reference APD for this modified configuration. The deviation distribution shown in Figure 3.23 is more well behaved than that of Figure 3.16. However, the overall deviation is roughly a factor of two larger for all axial positions. We believe this to be due to a combination of improper control rod modeling and associated spectral effects and is left for future work.

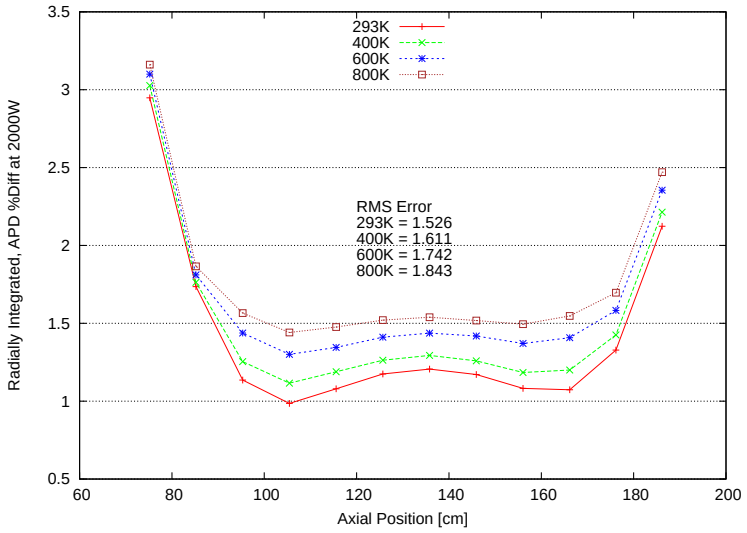

Figure 3.23: APD for the fully homogenized, modified minimum critical core configuration.

Table 3.21 shows the reaction rates and calculated eigenvalues for this core configuration.

By including the radial cross sections regions, improvements in capture and leakage rates can be seen when compared to that of Table 3.15.

Temp [K]	k_{eff} (pcm)	Diff Fiss Rate (%)	Diff Capt Rate (%)	Diff Leakage Rate (%)
293	1.01990 (1413.82)	-1.443	-8.363	29.852
400	0.99527 (1529.84)	-1.522	-8.541	29.857
600	0.95610 (1743.98)	-1.644	-8.816	29.727
800	0.92462 (1881.24)	-1.730	-9.004	29.876

Table 3.21: Diffusion results for the fully homogenized, modified minimum critical core configuration.

Table 3.22 shows the contribution percentage for the reaction rates as a function of temperature confirming spectral hardening for the modified configuration.

Temp [K]	Fission Rate Contrib. (%)	Capture Rate Contrib. (%)	Leakage Rate Contrib. (%)
293	41.97	46.30	11.79
400	40.96	46.97	12.13
600	39.35	48.05	12.65
800	38.05	48.88	13.11

Table 3.22: Percent contribution of individual reaction rates for the fully homogenized, modified minimum critical core configuration.

4 Discussion

In this section, observations based on the results of this work are presented.

4.1 Increased Deviation from Reference APD at Core Peripheries

A common observation in both the single assembly and minimum critical core calculations was an increased deviation from the reference APD core periphery near the fuel reflector interface. This increase was caused by flux weighting of the cross sections. Figure 2.3 shows that the flux gradient is highest near the peripheries of the fuel region approaching the reflector interface. In weighting this larger flux gradient, spatial fidelity of the cross sections is lost and calculated reaction rates in this region are less accurate. However, for all of the reported power distributions, the overall RMS error was well within physically measurable limits ($\pm$10%) and therefore no further axial cross section refinement was performed.

4.2 Flux Distribution in Reflector Regions

An example of inaccurate flux distributions within the reflector regions was shown in the results presented in Figure 3.18 and Table 3.17. For this homogenization of the minimum critical core configuration at 293K, the overall reported RMS deviation from the reference RPD is 0.223% while the differences from reference leakage and capture rates are 40.20% and -12.18%, respectively. Because of the simultaneous accurate power distribution and inaccurate integral reaction rates, it can be inferred that the flux distribution and reaction rates are preserved within the active core but lost in the reflectors outside of the core. The use of superhomogenized (SPH) cross sections [19] developed within MAMMOTH may improve this situation. By using these corrected cross sections, the reaction rates outside of the core can be preserved [18]. A more detailed discussion of SPH cross sections and their development is left for reference [19].

4.3 Diffusion Constant Treatment

The steady state multigroup neutron diffusion equation without delayed neutron treatment is shown in Equation 4.1.

$$-\nabla \cdot \mathbf{D}_g \nabla \phi_g + \Sigma_{r,g}\phi_g = \chi_g \sum_{g'} \nu\Sigma_{f,g'}\phi'_g + \sum_{g',g'\neq g} \Sigma_{s,g'\to g}\phi'_g \tag{4.1}$$

Within MAMMOTH, Rattlesnake solves this equation through the method of weighted residuals [41]. Using Gauss' Divergence theorem, the streaming term of Equation 4.1 is split into volumetric and surface terms forming Equation 4.2.

$$(\mathbf{D}_g \nabla \phi_g, \nabla \Psi) - \langle \mathbf{D}_g \nabla \phi_g, \Psi \rangle + \left(\sum_{r,g} \phi_g, \Psi \right) = \left(\chi_g \sum_{g'} \nu\Sigma_{f,g'}\phi'_g, \Psi \right) + \left(\sum_{s,g'\to g} \phi'_g, \Psi \right) \tag{4.2}$$

Focusing attention on the split streaming term on the left hand side of Equation 4.2, the volumetric term is calculated for each mesh element while the surface term is solved only where boundary conditions are applied. When modifying the diffusion coefficients in the optimization study discussed for each of the models within Section 3.1, the $D_x \nabla \phi_x$, $D_y \nabla \phi_y$, and $D_z \nabla \phi_z$ terms are adjusted.

$$-\mathbf{D}\nabla\phi(r) = -\mathbf{D}\left(\frac{\partial \phi}{\partial x}\hat{i} + \frac{\partial \phi}{\partial y}\hat{j} + \frac{\partial \phi}{\partial z}\hat{k} \right) \tag{4.3}$$

In the single assembly analysis, the $D_x \nabla \phi_x$ and $D_y \nabla \phi_y$ terms are assumed negligible due to the applied reflective radial boundary conditions. Due to the proximity of adjacent assemblies within the core configuration (40 mils between assemblies) it was also assumed that within this small distance the gradient in the x and y direction is also negligible. This implies that the diffusion study completed for the single assembly is applicable to the core analysis.

A possible improvement for the diffusion coefficient in future work would be to develop anisotropic, or directional, diffusion coefficients. In these, the individual parts of the diffusion coefficient in the x, y, and z directions are directly calculated. This allows for more accurate streaming and eliminates the need to artificially adjust the diffusion coefficient as done in this work. Several approaches are currently under development and are discussed below.

The first alternative is to develop a high fidelity, first order transport solver within MAMMOTH and use results from this simulation to back-calculate diffusion coefficients. The streaming term of the first order transport equation can be written in terms of the gradient of the current.

$$\begin{aligned}\boldsymbol{\Omega}\cdot\nabla\varphi\left(\mathbf{r},E,\boldsymbol{\Omega},t\right)&=\int_{4\pi}\boldsymbol{\Omega}\cdot\nabla\varphi\left(\mathbf{r},E,\boldsymbol{\Omega},t\right)d\boldsymbol{\Omega}=\nabla\cdot\int_{4\pi}\boldsymbol{\Omega}\varphi\left(\mathbf{r},E,\boldsymbol{\Omega},t\right)d\boldsymbol{\Omega}\\&=\nabla\cdot\int_{4\pi}j\left(\mathbf{r},E,\boldsymbol{\Omega},t\right)d\boldsymbol{\Omega}=\nabla\cdot J\left(\mathbf{r},E,t\right)\end{aligned}\tag{4.4}$$

Now using Fick's Laws, the gradient of the current can be related to the gradient of the flux multiplied by the diffusion coefficient.

$$\nabla\cdot J(r)=\nabla\cdot-D\nabla\phi(r)\tag{4.5}$$

Assuming that the diffusion coefficient is spatially independent within a region of interest (i.e. an element block as described in Section 2.2), an ad-hoc diffusion coefficient vector can be obtained [4].

$$D_k=\frac{J_k}{\left(\nabla\phi\right)_k};k=x,y,z\tag{4.6}$$

Once these anisotropic diffusion coefficients of Equation 4.6 are obtained, it is hypothesized that the full radial homogenization models will produce power distributions with sufficient accuracy. Taking the ad hoc relation even further, plans for a full Eddington tensor are also being developed [4]. Theoretically, by using this tensor, diffusion results would match those of high fidelity transport solutions.

The second methodology being employed in developing directional, anisotropic diffusion coefficients involves a collaboration with the Massachusetts Institute of Technology (MIT) and OpenMC. At the time of this writing, INL and MIT are currently working together to develop this capability for TREAT applications.

4.4 Control Assembly Effects

For each of the homogenizations in Section 3.2 it was shown that the control assembly location led to increased deviation from the reference APDs. For these models to be viable for future transient work, it is imperative that the control assemblies be more accurately modeled. Preliminary work is being completed on single control assembly calculations as well as 5x5 "minicores" to study interassembly spectral effects.

4.5 Albedo Boundary Conditions

Albedo boundary conditions are created by relating the incoming partial current to the outgoing partial current (Equation 4.7) [27].

$$\mathbf{J}_{\mathbf{g}}^{-}(E) = \boldsymbol{\alpha}(E)\,\mathbf{J}_{\mathbf{g}}^{+}(E) \tag{4.7}$$

where:

$\mathbf{J}_{\mathbf{g}}^{-}(E)$ and $\mathbf{J}_{\mathbf{g}}^{+}(E)$ are vectors of the multigroup partial currents.

$\boldsymbol{\alpha}(E)$ is a square matrix with a size equal to the number of groups and characterizes the albedo.

By invoking albedo boundary conditions, simulations of TREAT could theoretically be simplified to the active fuel. This would dramatically reduce computational cost in both the simulations within MAMMOTH as well as model construction within CUBIT. However, obtaining accurate albedo boundary conditions is not trivial and currently is not available within MAMMOTH. It is postulated that appropriate group-to-group albedo's can be obtained from Monte Carlo simulations or high fidelity transport simulations.

4.6 Applicability for Future Transient Calculations

One of the objectives of this research was to provide an accurate steady state model for future transient work. It was shown that diffusion theory performs well in reference to SERPENT solutions for obtaining accurate APDs in single assembly calculations. Each homogenization

produced, APD results were well within 1% of the reference SERPENT solutions. It can therefore be inferred that diffusion calculations are sufficient for single assembly transient calculations.

Diffusion calculations for the minimum critical core showed promising results through accurate RPDs and APDs near the center of the active core. However, before these models can be applied to transient applications, control assembly effects will need to be addressed. These effects were most pronounced in Figures 3.18 and 3.23.

5 Conclusions and Future Work

The main objectives of this work were to quantify various neutronic parameters for the minimum critical core configuration of the Transient Reactor Test Facility (TREAT). These parameters were calculated using the reactor physics package MAMMOTH within the MOOSE framework. For this work, only the neutron transport module, Rattlesnake, was utilized.

Cross sections used in this work were developed with SERPENT 2 using ENDF/B-VII.1 cross sections and are flux and volume weighted from full detail, 3D assembly models. It was shown that full 3D models were required for cross sections based on the scattering physics of this reactor. For full core calculations, the ratio of elastic to inelastic scattering decreases by 46.78% from that of the infinite lattice.

To most accurately quantify the neutron physics of the TREAT core, calculations were performed on single assemblies as well as full core configurations. For single assemblies, axial power distributions, eigenvalues, and reaction rates were figures of merit. For the full core calculations, axially integrated radial power distributions, radially integrated axial power distributions, eigenvalues, and reaction rates were figures of merit. All MAMMOTH calculated results were compared to reference SERPENT solutions.

It was shown for the single assembly calculations that by explicitly modeling the cooling channels and interassembly gaps, calculated power distributions are markedly improved. Results showed that the "full fuel homogenization with explicit channels" power distribution performed on par with more complex models. This homogenization produced an RMS difference from the reference APD of 0.076% with a modified isotropic diffusion coefficient. However, this homogenization did perform more poorly than more complex models for calculated integral reaction rates. It was shown that integral reaction rates were inaccurate when compared to reference SERPENT calculations up to -1.027% for the fission source, -0.750% for the capture rate, and -18.065% for the integral leakage while more complex approaches showed reaction rate inaccuracies up to 0.376% for fission rate, 1.559% for capture, and -10.571% for leakage. The observed deviations were due to inaccurate representations of the flux shape and diffusion coefficient treatment in the reflector regions.

As with the single assembly results, core configurations also produced enhanced accuracy

when the cooling channels and interassembly gaps were explicitly modeled. For this model, an RMS difference from the reference axially integrated RPD of 0.223% was observed. However, the integral reaction rates for this model were inaccurate. Because of the accurate power distribution, it can be inferred that the inaccuracies stem from inaccurate flux distrubtions within the radial and axial reflector regions - a behavior also observed in the single assembly calculations.

Future work will involve a more detailed analysis of diffusion coefficient treatment though anisotropic diffusion coefficients as well as better preserving the flux distributions within the reflector regions. Efforts are currently underway in both of these areas. Improved diffusion coefficients will be calculated from high fidelity first order transport solutions by equating the current to the gradient of the flux through Fick's law. Flux shape will be preserved in the future through the implementation of superhomogenized cross sections. It is expected that with these improvements, all of the target metrics will improve when compared to reference solutions.

Bibliography

[1] Argonne National Laboratory. PROTEUS, Simulation Tooset for Reactor Physics and Fuel Ccle Analysis. http://www.ne.anl.gov/pdfs/PROTEUSbrochure_v6.pdf.

[2] Y. Chang, P. Finck, and C. Grandy. Advnaced Burner Test Reactor Preconceptual Design Report - ANL-ABR-1. Technical report, Argonne National Laboratory, September 2006.

[3] M. D. DeHart and S. M. Bowman. Reactor Physics Methods and Analysis Capabilities in Scale. *Nuclear Technology*, 174:196–213, May 2011.

[4] M. D. Dehart and S. Schunert. Rattlesnake Updates to Improve TREAT Simulation Capabilities - INL/MIS-15-36598. Technical report, Idaho National Laboratory, September 2015.

[5] Department of Energy. Office of Nuclear Energy - Mission. http://www.energy.gov/ne/mission.

[6] Department of Energy. Transient Reactor Test Facility. http://energy.gov/sites/prod/files/TREAT%20Fact%20Sheet.pdf.

[7] T. Downar, D. Lee, Y. Xu, and T. Kozlowski. PARCS v2.6 U.S. NRC Core Neutronics Simulator THEORY MANUAL. Technical report, Purdue University, 2004.

[8] J. J. Duderstadt and L. J. Hamilton. *Nuclear Reactor Analysis*. John Wiley S Sons, Inc., 1976.

[9] G. A. Freund, P. Elias, D. R. MacFarlane, J. D. Geier, and J. F. Boland. Design Summary Report on the Transient Reactor Test Facility TREAT, ANL-6034. Technical report, Argonne National Laboratory, June 1960.

[10] D. Gaston, C. Newman, G. Hansen, and D. Lebrun-Grand'e. MOOSE: A parallel computational framework for coupled systems of nonlinear equations. *Nuclear Engineering Design*, 293:1768–1778, 2009.

[11] F. N. Gleicher, J. Ortesi, B. W. Spencer, Y. Wang, S. R. Novascone, J. D. Hales, D. Gaston, R. L. Williamson, and R. C. Martineau. The Coupling of the Neutron Transport Application RATTLESNAKE to the Fuels Performance Application BISON Under the MOOSE Framework. *International Conference on Reactor Physics (PHYSOR 2014)*, 2014.

[12] S. Goluoglu and H. L. Dodds. A Time-Dependent, Three-Dimensional Neutron Transport Methodology. *Nuclear Science and Engineering*, 139(3):248–261, April 2001.

[13] S. Goluoglu, J. Paluch, M. DeHart, and S. Morrell. TDKENO: A Hybrid Time-dependent Transport Analysis Tool. *Transactions of American Nuclear Society*, 111:1401–1404, November.

[14] S. Goluoglu, L. M. Petrie Jr., M. E. Dunn, D. F. Hollenbach, and B. T. Rearden. Monte Carlo Criticality Methods and Analysis Capabilities in SCALE. *Nuclear Technology*, 174(2):214–235, May 2011.

[15] D. Gray, A. McCaughan, and B. Mookerji. Crystal Structure of Graphite, Graphene and Silicon. *Physics for Solid State Applications*, 6.730.

[16] T. Hamidouche, A. Bousbia-Salah, E. K. Si-Ahmed, M. Y. Mokeddem, and F. D'Auria. Application of coupled code technique to a safety analysis of a standard MTR research reactor. *Nuclear Engineering and Design*, 239:2104–2118, 2009.

[17] H. L. Hanshaw, A. Haghighat, and J. C. Wagner. Multigroup Cross Section Generation with Spatial and Agular Adjoint Weighting. Technical report, Penn State University.

[18] A. Hébert and A. Kavenoky. Development of the SPH Homogenization Method. *Proc. Int. Topl. Mtg. Advances in Mathematical Methods for the Silution of Nuclear Engineering Problems*, 1:195, April 1981.

[19] A. Hébert and G. Mathonnière. Develpoment of a Third-Generation Superhomogeneisation Method for the Homogenization of a Pressurized Water Reactor Assembly. *Nuclear Science and Engineering*, 115:129–141, April 1993.

[20] IAEA. Evaluation of High Temperature Gas Coled Reactor Performance: Benchmark Analysis Related to Initial Testing of the HTR and HTR-10, IAEA-TECDOC-1382. Technical report, 2003.

[21] Alternative Analysis for the Resumption of Transient Testing Program, INL/EXT-13-28597. Technical report, November 2013.

[22] S. T. Keller. Modeling the Oregon State University TRIGA Reactor Using the Attila Three-Dimensional Deterministic Transport Code. Master of Science Thesis, Oregon State University, 2007.

[23] F. Kirn, J. Boland, H. Lawroski, and R. Cook. Reactor Physics Measurement in TREAT, ANL-6173. Technical report, October 1960.

[24] T. Kozlowski, R. M. Miller, and T. J. Downar. Consistent Comparison of the Codes RELAP5/PARCS and TRAC-M/PARCS for the OECD MSLB Coupled Code Benchmark. *Nuclear Technology*, 146:15–28, 2003.

[25] J. R. Lamarsh. *Introduction to Nuclear Reactor Theory.* Addison-Wesley, 1966.

[26] J. R. Lamarsh and A. J. Baratta. *Introduction to Nuclear Engineering* . Prentice-Hall, Inc., 3 edition, 2001.

[27] E. E. Lewis and W. F. Miller Jr. *Computational Methods of Neutron Transport.* American Nuclear Society, 555 N. Kensington Avenue, La Grange Park, IL 60525, 1993.

[28] D. Lucas, H. Gougar, P. Roth, T. Waring, G. Faila, J. McGhee, and A. Barnett. Applications Of The 3-D Deterministic Transport Attila For Core Safety Analysis. Technical report, Idaho National Engineering and Environmental Laboratory, October 2004.

[29] D. Lucas, H. Gougar, T. Waring, G. Faila, J. McGhee, D. A. Barnett, I. Davis, and D. Lucas. Comparison Of The 3-D Deterministic Neutron Transport Code Attila To Measure Data, MCNP and MCNPX For The Advanced Test Reactor. Technical report, Idaho National Laboratory, September 2005.

[30] P. B. Lyons. Mission Need Statement For the Resumption of Transient Fuel Testing. Technical report, Office of Nuclear Energy, U.S. Department of Energy, 2010.

[31] G. Marleau. Dragon Theory Manual, Part 1: Collision Probability Calculations, IGE-236 Revision 1. Technical report, École Polytechnique de Montréal, October 2001.

[32] G. Marleau, A. Hébert, and R. Roy. A User Guide For DRAGON, IGE-174 Rev. 12 (Release 3.06L. Technical report, École Polytechnique de Montréal, July 2013.

[33] R. Morris. *CUBIT 15.0 User Documentation*. ETI, UT.

[34] C-Elemental(n,total). `http://www.nndc.bnl.gov/sigma/getPlot.jsp?evalid=14971&mf=3&mt=1&nsub=10`. [NNDC online].

[35] PARCS-NRC. `http://www.nrc.gov/about-nrc/regulatory/research/safetycodes.html`. [NRC online].

[36] Oak Ridge National Laboratory. *Getting Started wiht Scale 6.1*.

[37] D. Okrent, C. E. Dickerman, J. Gasidlo, D. M. O'Shea, and D. F. Schoeberle. The Reactor Kinetics of the Transient Reactor Test Facility (TREAT) ,ANL-6174. Technical report, Argonne National Laboratory, 1960.

[38] J. Ortensi, A. Alberti, Y. Wang, F. Gleicher, S. Schunert, and T. Palmer. Methodologies and Requirements for the Generation of Physics Data Inputs to MAMMOTH Transient Simulations in Support of the Transient Reactor Test Facility - INL/LTD-15-36265. Technical report, Idaho National Laboratory, September 2015.

[39] J. Ortensi, M. D. DeHart, F. N. Gleicher, Y. Wang, and A. L. Alberti. Full Core TREAT Kinetics Demonstration Using Rattlesnake/BISON Coupling Within MAMMOTH,INL/EXT-15-36268. Technical report, Idaho National Laboratory, August 2015.

[40] L. A. Schoof and V. R. Yarberry. EXODUS II: A Finite Element Data Model, SAND92-2137. Technical report, Sandia National Laboratory, December 1995.

[41] S. Schunery, Y. Wang, and R. Martineau. A New Mathematical Adjoint for the Modified SAAF-S_N Equations. Technical report, Idaho National Laboratory.

[42] Serpent, a Continuous-energy MinteCarlo Reactor Physics Burnup Calculation Code. `http://montecarlo.vtt.fi/`. [VTT Technical Research Centre of Finland].

[43] E. R. Shemon, M. A. Smith, and C. Lee. PROTEUS-SN Methodology Manual. Technical report, Argonne National Laboratory, June 2014.

[44] K. S. Smith. Spatial Homogenization Methods for Light Water Reactor Analysis. Ph.D. Dissertation, Massachisetts Institute of Technology, 1980.

[45] T. Takeda and H. Ikeda. 3-D Neutron Transport Benchmarks. *Nuclear Science and Technology*, 28:656–669, 1991.

[46] J. Thomas. Advanced Multi-Physics Modeling and Simulation Efforts for Fast Reactors. Technical report, Argonne National Laboratory, April 2014.

[47] Final Environmental Assessment for the Resumption of Transient Testing of Nuclear Fuels and Materials. Technical report, February 2014.

[48] R. L. Williamson, J. D. Hales, S. R. Novascone, M. R. Tonks, D. R. Gatson, C. J. Permann, D. Andrs, and R. C. Martineau. Multidimensional Multiphysics Simulation of Nuclear Fuel Behavior. *Journal of Nuclear Materials*, 423:149–163, January 2012.

[49] W. Yang, M. Smith, C. Lee, A. Wollaber, D. Kaushik, and A. Mohamed. Neutronics Modeling and Simlation of SHARP for Fast Reactor Analysis. *Nuclear Engineering and Technology*, 42:520–545, 2010.

[50] T. Zhou. Benchmarking Thermal Neutron Scattering in Graphite. Ph.D. Dissertation, North Carolina State University, 2006.

APPENDICES

A Cost and Risk Analysis of TREAT and ACRR

Life-cycle cost estimates are broken down into four catagories: 1) program cost for the Resumption of Transient Testing Program (RTTP), 2) 40 year operations cost, 3) science coordination, and 4) decontamination and decommission.

The RTTP cost for TREAT includes assessment, refurbishment, and/or replacement of all equipment. RTTP cost for ACCR includes the construction of a new hot cell and installation of a fuel motion monitoring system. Science coordination includes the completion of an experimenter's guide and the funding for a test program coordinator [21].

Table A.1 shows the cost breakdown of the TREAT and ACRR facilities. The cost range shown has uncertainty levels of -20% to +35% [21].

Catagory	TREAT (millions)	ACRR (millions)
RTTP	\$56 to \$90	\$167 to \$279
40 Year Operations Cost and Decontamination and Decommission	\$439 to \$741	\$389 to \$656
Science Coordination	\$31 to \$53	\$31 to \$53
Total LCC Estimate	\$526 to \$884	\$587 to \$988

Table A.1: LCC Comparison for TREAT and ACRR

The overall cost of operations of the two facilities are similar. This is caused by two nearly offsetting categories: RTTP and operations. The ACRR RTTP cost is significantly higher than TREAT due to the requirement of constructing a hot cell and fuel motion monitoring system. However, the operating costs of ACRR is far less than TREAT due to the fact that ACRR supports multiple customers outside of DOE-NE.

Nine specific risks were evaluated for the TREAT and ACRR facilities [21].

Risk Description	TREAT Score	ACRR Score	Explanation
Significant Impact to Env. Discriminators	0.33	0.60	TREAT - low air and water emissions. ACRR - low air and water emissions, requirement of new hot cell
Impact to Health and Safety of Public	0.00	0.67	TREAT - no use of public roads. ACRR - requires use of public roads for transport of irradiated materials.
Impact to Health and Safety of Workers	0.67	0.67	TREAT - requires additional rad workers to operate reactor. ACRR - requires additional radiation workers to operate new hot cell.
Impact to safeguards, security, and proliferation	0.00	0.67	TREAT - no use of public roads. ACRR - requires use of public roads for transport of irradiated materials.
Technical Performance	0.10	0.30	TREAT - limited experienced personnel for reactor operations. ACRR - requires installation of fuel motion monitoring device and hot cell.
Cost	0.85	0.76	TREAT - uncertainty with refurbishing cost. ACRR - uncertainty of cost of hot cell and fuel motion monitoring device
Inability to perform experiments efficiently	0.00	0.67	TREAT - dedicated transient testing facility. ACRR - requires coordination with other customer and transportation needs.
Failure to meet RTTP capability	0.20	0.50	TREAT - uncertainty with timetable for refurbishment. ACRR - uncertainty with timetable for installation of hot cell and fuel motion monitoring device.
Impact on other dependent facilites or users	0.10	0.50	TREAT - required coordination with Hot Fuel Examination Facility (HFEF). ACRR - required coordination with other customer needs, transportation, and HFEF.
Total Risk Score	2.25	5.34	

Table A.2: Risk Scoring of TREAT and ACRR.

Based on the results of Table A.2 and a complementary sensitivity analysis of those results, TREAT was the highest scoring alternative and determined to hold the highest value to the government for the RTTP [21].